Remote Sensing of Environment 290 (2023) 113546

Contents lists available at ScienceDirect

Remote Sensing of Environment

journal homepage: www.elsevier.com/locate/rse

Monitoring erosion in tropical savannas from C-band radar coherence

Pascal Castellazzi [a,*], Sana Khan [b], Simon J. Walker [c], Rebecca Bartley [d], Scott N. Wilkinson [c], Jonathan C.L. Normand [e]

[a] Commonwealth Science and Industrial Research Organisation (CSIRO), Deep Earth imaging FSP, Environment, Waite Rd, Urrbrae, SA 5064, Australia
[b] Commonwealth Science and Industrial Research Organisation (CSIRO), Environment, 1 James Cook Dr, Douglas, QLD 4814, Australia
[c] Commonwealth Science and Industrial Research Organisation (CSIRO), Environment, GPO Box 1700, Canberra, ACT 2600, Australia
[d] Commonwealth Science and Industrial Research Organisation (CSIRO), Environment, GPO Box 2583, Brisbane, QLD 4001, Australia
[e] University of Southern California, Viterbi School of Engineering, Los Angeles, CA, USA

ARTICLE INFO

Edited by Jing M. Chen

Keywords:
Geomorphic change detection
Deposition
River management
Radar interferometry
InSAR
Australia

ABSTRACT

Increased erosion related to climate and/or land cover change has adverse impacts on terrestrial and aquatic ecosystems. Mapping of erosion hotspots improves our ability to identify and potentially remediate the most active erosion sources. The topical savannas of the Great Barrier Reef catchments, in northeast Australia, are generating excessive sediment yields, primarily from gully erosion. To reduce the adverse impacts on marine ecosystems, there is an urgent need to identify priority erosion hotspots and implement mitigation measures. While repeat airborne LiDAR surveys allow subtle topographic change detection, they are cost-intensive for catchment-scale applications and their applicability is constrained by data avalability and detection treshold of ground level change. In contrast, satellite-based radar imagery can allow large scale tracking of geomorphic change at high temporal resolution. Here we apply a new method based on Sentinel-1 C-band radar images and Coherence Change Detection (CCD), where large stacks of interferometric coherence images are subdivided with rain gauge time-series for separation of erosion-rich and erosion-free coherence information. After correcting the former with the latter, the resulting corrected coherence maps are compared with differential elevation models derived from multitemporal LiDAR, regional scale gully delineation maps, maps of gullying potential and in-situ field verification. Our results demonstrate the promising potential of this technique in detecting gully erosion hotspots. The coherence loss indicating erosion/deposition is well detected in wide gully morphologies, however, the line-of-sight angle does not allow penetration into narrow linear gullies. Further, CCD detects sheetwash or rill erosion occurring in areas identified as at risk of gully expansion, which is commonly below detection threshold for multitemporal LiDAR datasets. When used with LiDAR-derived geomorphic change mapping and gullying potential maps, CCD allows identification of gully erosion dynamics and forecasting gully evolution and creation, which is critical for supporting mitigation measures.

1. Introduction

At geologic timescales, cycles of erosion and deposition are key drivers of landscape evolution that shape the Earth's surface (Dietrich et al., 2013; Dietrich and Perron, 2006; Phillips, 2021; Summerfield, 2014). The last few decades of anthropogenic activities have significantly altered this process of sediment generation, transportation, and deposition (Steffen et al., 2015, 2018). Key anthropogenic drivers of erosion include land use change, dam construction and water abstraction/diversion (Kondolf, 1997; Kondolf et al., 2018, 2022; Qin et al., 2019; Vorosmarty, 2000). Against the backdrop of changing climate, this dynamic cycle of landscape erosion has further accelerated with deleterious effect on hydrological, geomorphic, and ecological river health. The dynamics of this terrestrial erosion determines the fate of the aquatic water bodies into which they eventually drain (Bainbridge et al., 2021; Bartley et al., 2015; Kondolf et al., 2022; Tangi et al., 2022). Therefore, for sustainable management of terrestrial and aquatic environmental assets, there is an urgent need to identify hotspots of erosion for targeted management practices.

Typically, landscape erosion is assessed using empirical and physical

* Corresponding author.
E-mail addresses: Pascal.Castellazzi@csiro.au (P. Castellazzi), Sana.Khan@csiro.au (S. Khan), Simon.Walker@csiro.au (S.J. Walker), Rebecca.Bartley@csiro.au (R. Bartley), Scott.Wilkinson@csiro.au (S.N. Wilkinson), normand@usc.edu (J.C.L. Normand).

https://doi.org/10.1016/j.rse.2023.113546
Received 12 August 2022; Received in revised form 27 February 2023; Accepted 11 March 2023
Available online 24 March 2023

models. These models often integrate remotely sensed datasets with field observations to assess catchment-scale forms and processes (Coulthard et al., 2013; McCloskey et al., 2021; Schmitt et al., 2018). Recent advances in remote sensing techniques, improved public availability of spatial datasets, and enhanced computing resources have enabled such landscape assessment at unprecedented scales (Vrieling, 2006; Piégay et al., 2020). Further, availability of multi-temporal datasets (repeated LiDAR based Digital Elevation Models and satellite imagery) has opened avenues for understanding the dynamic cycle of erosion and deposition that can be used for tracking the active provenance and fate of sediment (Schmitt et al., 2016; Tangi et al., 2022).

Radar imagery products, particularly interferometric coherence images (Zebker and Villasenor, 1992), allow identification of subtle changes of the ground's scattering properties. Erosion and deposition changes microtopography, which modifies the structure of scattering targets and changes the radar signal amplitude and phase. This leads to a reduced coherence value between the initial and the eroded state for the corresponding pixels. Thus, information related to erosion/deposition is concentrated in coherence images formed by comparing pairs of images acquired before and after geomorphic change events. Hence it can be highlighted through a range of techniques referred to as Coherence Change Detection (CCD). Typically, coherence information related to erosion appears with different temporal behaviour in coherence image time-series than the transient coherence loss due to soil moisture (Scott et al., 2017; Jordan et al., 2020) and with different spatial patterns than anthropogenic disturbances (e.g., Liu et al., 2001, in which geophysical survey lines were identified). In some cases, aeolian erosion processes and water-facilitated weathering can be discriminated in a coherence image stack constrained by meteorological data (Schepanski et al., 2012).

Interferometric SAR and CCD techniques have been applied in several regions of the world for erosion mapping efforts: in Algeria (Liu et al., 2001), Morocco (Schepanski et al., 2012), Chile (Cabré et al., 2020), Mongolia (Kim et al., 2020, 2021), Peru (Lefort et al., 2004); Spain (Liu et al., 1999, 2004), Argentina (Olen and Bookhagen, 2020), Iceland (Smith et al., 2000), the USA (Wegmuller et al., 2000) and China (Jiang et al., 2021). Earlier studies used radar data from the first (e.g., ERS) and second (e.g., ENVISAT) generations of radar satellites and typically interpret the coherence of few selected interferometric pairs (Liu et al., 1999, 2001, 2004; Lefort et al., 2004, Schepanski et al., 2012). These studies were limited by the low repeat path frequency of the 1st and 2nd generations of radar satellites (typically 35 or 24 days) and by the limited spatial and temporal coverage available. Most recent studies take advantage of the higher repeat path frequency (6 to 12 days) and the global spatial coverage of Sentinel-1 (Cabré et al., 2020; Olen and Bookhagen, 2020; Kim et al., 2020) to improve characterisation of erosion in time and space. Several of the CCD studies have used validation data to help interpret the signal decorrelation highlighted by coherence images, which can be affected by any kind of surface disturbance that occurred between the two acquisition dates. This includes difference of Digital Elevation Models (DEM; Kim et al., 2020), optical imagery (Liu et al., 2001, 2004; Cabré et al., 2020; Olen and Bookhagen, 2020), meteorological data (Cabré et al., 2020; Schepanski et al., 2012; Olen and Bookhagen, 2020), geomorphological maps (Liu et al., 2004; Olen and Bookhagen, 2020) and field observation (Cabré et al., 2020). While few applications of deformation-mapping based on Interferometric SAR (InSAR) have been published in Australia in the recent years (Castellazzi and Schmid, 2021; Castellazzi, 2021; Parker et al., 2021a,b), there is no publication on InSAR CCD over Australia available to this date. Further, there are no studies that have used CCD for detecting erosion hotspots in gullied landscapes. Although CCD is not a novel technique, its application for detecting geomorphic change in gullied landscapes is unexplored to this date.

Recent radar imagery products such as Sentinel-1 are publicly available over any location in the World. Over most regions, time-series of 150–200 repeat-path images acquired in the period 2016–2021 are available in at least one orbital direction (descending or ascending). This allows several options of connection-graph designs to create stacks of interferometric coherence images (Fig. 1), each related to a certain computing effort and allowing different observations. Most erosion studies (e.g., Olen and Bookhagen, 2020) follow a time-line design (Fig. 1A), where coherence images are only calculated between temporally adjacent radar images. This design implies a relatively low computer effort and allows coherence observations at the minimum time intervals. Studies characterising the coherence decay and its deviation (for identification of loss beyond a normal background coherence decay curve) use a single-master approach (Fig. 1B, e.g., Jordan et al., 2020). Full or SBAS stacks (Fig. 1C-D) are commonly used in interferometric ground deformation mapping (e.g., SBAS stack, in Australia: Castellazzi and Schmid, 2021) and allows a varying degree of redundancy useful to extract noise and artefacts via stacking (Berardino et al., 2002; Bui et al., 2020). The benefits of such coherence stack design have not been tested for erosion mapping to date.

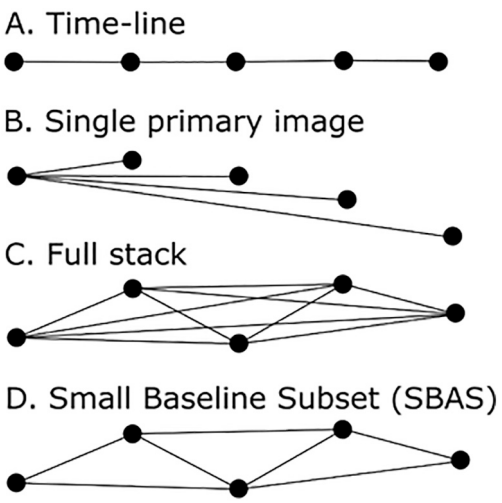

Fig. 1. Typical strategies for creating coherence image stacks from radar image time-series. Each segment corresponds in a coherence image obtained between two radar acquisitions. This example contains only 5 images, with connection strategies creating 4, 4, 10 and 7 coherence images, respectively. Note that the quantity of coherence images produced by strategy D depends on the temporal and spatial baseline thresholds used.

There is considerable interest in identifying and treating the major sources of fine sediment and associated particulate nutrients draining from land-based sources to the Great Barrier Reef (GBR) lagoon (Waterhouse et al., 2017). Gully erosion is the major erosion process responsible for the excess sediment delivery to the GBR (Wilkinson et al., 2013; Bartley et al., 2014; McCloskey et al., 2021), and the area occupied by gullies is estimated to have increased ~10-fold since European settlement in parts of North-eastern Australia (Shellberg et al., 2010). The increase in gully erosion is linked to anthropogenic activities such as over-grazing and mining, particularly when located on vulnerable soil types (Bartley et al., 2018; Lewis et al., 2021).

Evaluating the rates of gully erosion in the GBR catchments has been assessed using a range of techniques including erosion pins (Wilkinson et al., 2018), photogrammetry (Koci et al., 2017), terrestrial laser scanning (Goodwin et al., 2017; Kinsey-Henderson et al., 2021) and airborne LiDAR (Khan et al., 2023). Despite these methods being useful for assessing fine scale erosion processes, they have two important limitations: (1) the small spatial scale over which they can be applied, generally restricting assessments to individual gullies or small sub-catchments and (2) the availability of LiDAR datasets and the cost to acquire new ones. To help identify and target areas of active gully erosion for rehabilitation prioritisation (Darr and Pringle, 2017), as well as provide baseline assessments of active gully erosion over whole

catchments, there is a need to develop techniques that can be applied over larger spatial scales (> 10,000 km^2).

The recent, global availability of open-access Sentinel-1 radar imagery is a game-changer, as it allows CCD techniques to be implemented over large-scales, creating an opportunity for regional to continental-scale erosion mapping. In GBR catchments, sediment tracing using fallout radionuclides has identified gully erosion as a larger contributor of fine sediment to rivers and marine systems than surface soil erosion (Wilkinson et al., 2013). However, identifying and distinguishing active from inactive gully erosion has been challenging over large spatial areas. Thus, this study presents an ideal case to test the capability of radar CCD techniques based on Sentinel-1 data. If successful, the method may enable the identification of active gully erosion over entire catchments in the GBR.

There are two main aims of this study. Firstly, to test a systematic approach for CCD-based detection of erosion/deposition at temporal scales ranging from individual rain events to several years. Secondly, to understand the advantages and limitations of the technique and its value added to replace or complement existing erosion mapping techniques. This is supported by a series of auxiliary observation including (1) LiDAR-derived DEMs of Difference, (DoD) erosion rates (2) regional scale gully delineation, (3) gullying risk maps derived from several existing gully sites with independent, LiDAR-derived validation data and (4) in-situ field validation. The independent field sites selected for this study represent a range of gully shapes and morphologies from small linear hillslope gullies of width 5–25 m to large wide gullies of width 150–300 m in deep alluvium (Thwaites et al., 2022), thereby providing a useful test of this technique for a range of erosional features.

2. Study areas

The two study areas are tropical savannah environments, located within the Burdekin Catchment, which extends over ~130,000 km^2 and drains into the Great Barrier Reef (GBR) Lagoon south of Townsville on the east coast of Australia (Fig. 2). Study area 1 is located ~20 km (north-east corner) South-west of the City of Townsville, Queensland, Australia, and extends as far as 115 km (south-west corner). Study area 2 is located ~100 km south-east of Townsville and extends as far as 215 km. For both areas, the annual precipitation is in the range 500–800 mm/yr, with a strong east-west gradient and decreasing annual precipitation rates progressing inland. The area has a hot, semi-arid climate with two seasons: a short, wet season focused on December to March and a long, warm, and dry season the rest of the year (Jarihani et al., 2017). Bare soil, low-density eucalypt open woodlands and tropical savannah are the dominant land cover types (Fig. 3).

The Burdekin catchment is the largest contributor of anthropogenic derived fine sediment to the GBR (Bainbridge et al., 2018; Mariotti et al., 2021), and has some of the highest gully densities and cross-sectional areas of any of the GBR catchments (McCloskey et al., 2021). The sites selected for this study have been part of other existing long-term monitoring assessments of gully erosion (Wilkinson et al., 2018) and gully rehabilitation effectiveness (e.g., Koci et al., 2021) and had suitable gully mapping and erosion data from lidar DEM analysis to enable technique validation (Walker et al., 2020; Khan et al., 2023).

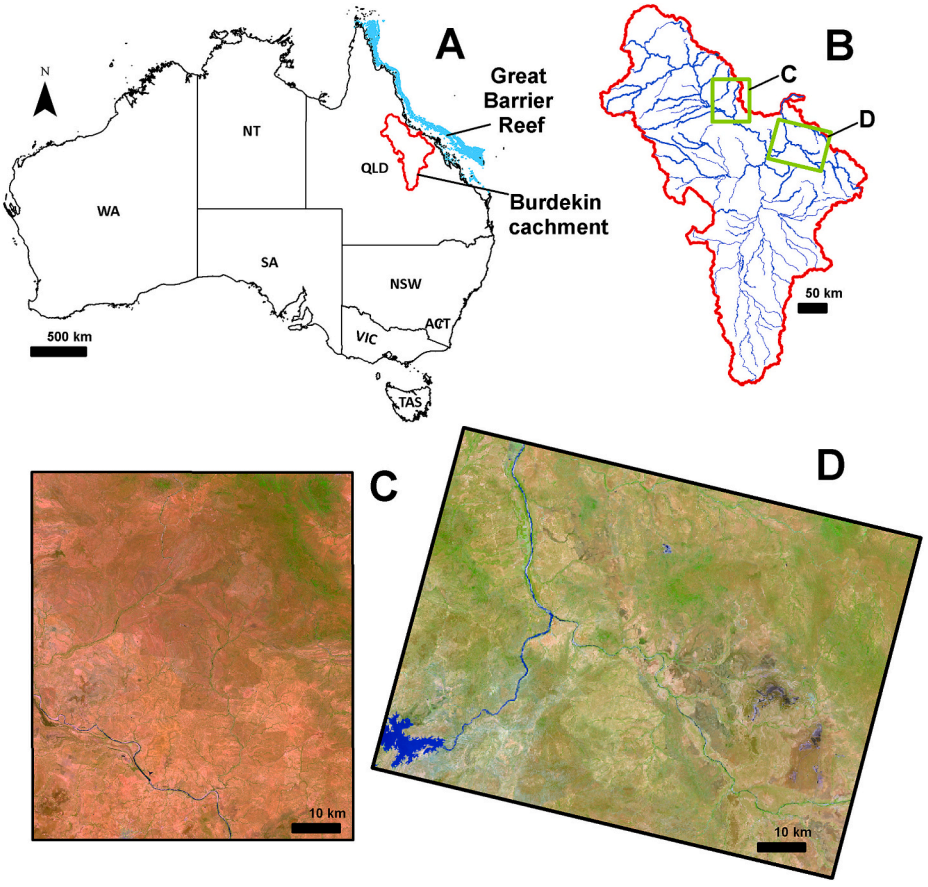

Fig. 2. Location of the two study areas, location of the Burdekin catchment (A) and location of the study area in the Burdekin catchment (B), with the main drainage lines. Presentation of the radar imagery processing footprints (C, D) with two cloud-free, 'barest earth' optical images derived from Roberts et al. (2019).

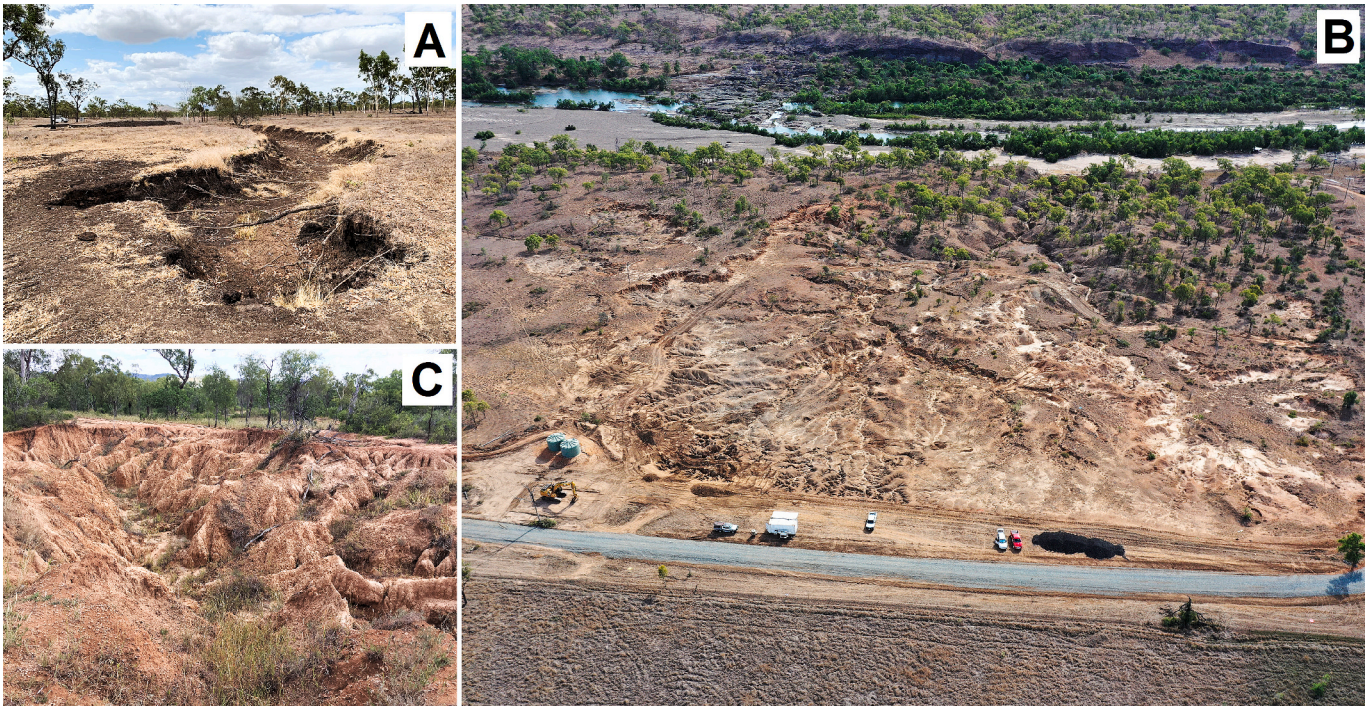

Fig. 3. Photos of the active erosional features represented by contrasting gully types in the study area 2: (A) Linear gully at Strathbogie, (B) Alluvial gully and gullied landscape viewed from above at Glen Bowen, (C) Linear-alluvial gully at Mount Wickham. Photos by Fruition Environmental and NQ Dry Tropics.

Table 1
Characteristics of the radar image time-series used in this study.

Study areas	Sentinel-1 orbital track	Time-series start/end		Number of images/coherence maps	Extent (km^2)
1 - Fig. 2C	89	2016-08-01	2021-09-28	156/755	5006
2 - Fig. 2D	16	2016-07-27	2021-09-23	156/758	7015

3. Materials and methods

3.1. Radar imagery and processing

Sentinel-1 C-band Interferometric Wide (IW) Synthetic Aperture Radar (SAR) image tiles were downloaded from the Alaskan Satellite Facility (ASF) web portal. Radar imagery processing was performed using ENVI 5.6 and SARSCAPE 5.6. Hundreds of Sentinel-1A image tiles corresponding to two adjacent descending swaths and to 156 acquisition dates were downloaded (Table 1). For both swaths, tiles were merged, and one spatial subset was extracted for each swath (Fig. 2; Table 1). A multilooking factor of 3/1 in Range/Azimuth was applied to improve the signal-to-noise ratio and produce images with near-square pixel ground footprints with a resolution in the range [15–20] meters. All radar image pairs with temporal baselines of equal or below 60 days, and with spatial baselines below 3% of the critical baseline were created, following a typical SBAS connection graph design (Berardino et al., 2002; Fig. 1). The interferometric coherence was computed for each selected image pair using a typical 5 × 5 pixel windows and the resulting coherence maps were projected onto 20-m georeferenced rasters using the AW3D30 Digital Elevation Model v3.1 (Takaku et al., 2020). The end-product of the radar processing is two georeferenced interferometric coherence data cubes with 755 and 758 coherence maps.

3.2. Precipitation data

Daily precipitation time-series from in situ rain gauges at three locations (Table 2) were downloaded from the Australian Bureau of Meteorology's Climate Data portal (BOM; http://www.bom.gov.au/climate/data/). The datasets were manually selected from all available rain gauge data for their completeness during the study period (100% of the days covered) and their geographical location inside the two study areas. Two rain gauges time series are used for the study area 1, as they are located at the extreme North and South end of the area. Only one rain gauge dataset is used for the study area 2, located close to its center (Fig. 4).

3.3. Validation data

To validate the results, four types of data and observations are compared with results from the CCD technique: (1) DEMs of Difference (DoD), (2) LiDAR-based and in situ gully delineation (GD), (3) gullying potential maps (GP), and (4) in-situ field observations (FO). A summary of these datasets, including the rain gauges, is presented in Table 2. A detailed description of the three DoD datasets is presented in Table 3, and maps with locations of the datasets across the two study areas is presented in Fig. 3.

Table 2
Type, location, coverage, and source of auxiliary data used in this study.

Data type and location name (Fig. 3)	Study area	Lat/Lon coordinates	Approx. coverage	Source
Rain Gauges (RG)				
Charters Towers Airport (34084)	1	−20.05/146.27	Point data	BOM
Woolshed (33307)	1	−19.42/146.54	Point data	BOM
Strathmore (33082)	2	−20.50/147.63	Point data	BOM
DEM of Difference (DoD)				
Main Creek	1	−19.82/146.57	15 km^2	Unpublished analysis
Mt Wickham	2	−20.47/147.41	0.03 km^2	Khan et al., 2023
Glen Bowen	2	−20.56/147.59	0.03 km^2	Khan et al., 2023
Strathbogie	2	−20.20/147.59	0.19 km^2	Khan et al., 2023
Regional-scale Gully Delineation (GD)				
Red Hill Creek	2	−20.33/147.27	25 km^2	Walker et al. (2020, 2022)
Collinsville	2	−20.67/147.79	19 km^2	Daley et al. (2021)
Gullying Potential (GP)				
Weany creek 1	1	−19.89/146.53	6 km^2	Walker et al. (2020, 2022)
Weany creek 2	1	−19.83/146.57	6 km^2	Walker et al. (2020, 2022)
Bogie	2	−20.15/147.50	15 km^2	Walker et al. (2020, 2022)
Field Observation (FO)				
Weany creek 3	1	−19.89/146.515	2 km^2	Field survey in October 2022

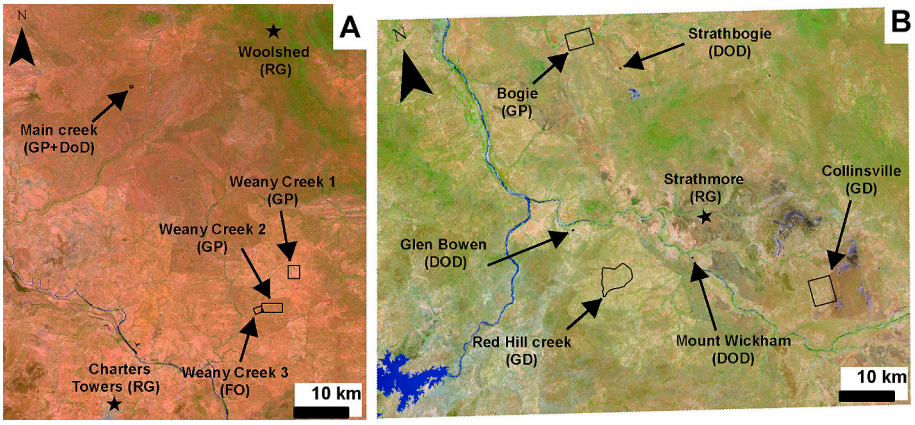

Fig. 4. Location of the rain gauges and of the validation datasets used in Study area 1 (A) and 2 (B). Nomenclature: RG: Rain Gauges; DoD: DEM of Difference; GD: in situ Gully Delineation, GP: Gullying Potential from Walker et al. (2020, 2022). (B) is rotated anticlockwise (−15 degrees) for presentation.

Table 3
Soil, lithology, precipitation, or other contextual information for the three DoD datasets used to validate the results over the Study area 2.

DoD Site	Main Creek	Mt Wickham	Glen Bowen	Strathbogie
Study area	1	2	2	2
Gully characteristics	Linear: Gully area focused on a distinct narrow trunk stream along the hillslope with minor secondary channels	Linear-alluvial: Wide gullies along distinct trunk stream	Alluvial: Wide gully area along trunk stream and multiple secondary channels	Linear: Gully area focused on a distinct trunk stream along the hillslope with minor secondary channels
Soils	Red Chromosol	Hypernatric Brown Sodosol	Sodic Hypocalcic Red Dermosol	Black Vertosol
Geology	Granodiorite	Granite and Granodiorite	Granodiorite	Granite, Basalt
Terrain (% slope property)	3%	10%	3–4%	6–7%
Average annual long-term rainfall (mm)	~780 mm	~600 mm	~ 880 mm	~ 750 mm
Vegetation over-story	Widely spaced Narrow-leafed Ironbark and Bloodwood	Widely spaced Narrow-leafed Ironbark and Bloodwood + Popular gum	Widely spaced Narrow-leafed Ironbark and Bloodwood	Widely spaced Narrow-leafed Ironbark and Bloodwood
Vegetation groundcover	Dominated by native perennial grasses	Dominated by Indian Couch	Dominated by Indian Couch	Dominated by Indian Couch
Length and dates of DoD (dd/mm/yyyy)	~7.83 years 07–08 November 2013 and 07 August 2021	~2.83 years 13–19 September 2018 and 19–20 July 2021	~2.83 years 13–19 September 2018 and 19–20 July 2021	~2 years 26–27 July 2019 and 19–20 July 2021
DEM resolution	2013 & 2021–0.5 m	2018 & 2021–0.5 m	2018 & 2021–0.5 m	2019 & 2021–0.5 m
1st DEM accuracy	Horizontal accuracy of 0.80 m & vertical accuracy of 0.30 m	Horizontal accuracy of 0.80 m & vertical accuracy of 0.30 m	Horizontal accuracy of 0.80 m & vertical accuracy of 0.30 m	Horizontal accuracy of 0.80 m & vertical accuracy of 0.30 m
2nd DEM accuracy	Horizontal accuracy of 0.3 m & vertical accuracy of 0.1 m	Horizontal accuracy of 0.3 m & vertical accuracy of 0.1 m	Horizontal accuracy of 0.3 m & vertical accuracy of 0.1 m	Horizontal accuracy of 0.3 m & vertical accuracy of 0.1 m

3.4. Approach

InSAR coherence maps are interpreted considering three main influencing contributors to the total interferometric coherence (γ_{tot}) calculated from two radar image acquisitions (Eq. 1), similarly to Jordan et al. (2020) and first expressed by Zebker and Villasenor (1992). This study being based on imagery from a 3rd generation SAR sensor with relatively small spatial baselines and well-controlled radiometric parameters, their influence is considered negligeable.

$$\gamma_{tot} = \gamma_b + \gamma_t + \gamma_p \quad (1)$$

Where γ_b is the background coherence loss corresponding to the typical decay of coherence over time due to time-dependant, progressive, structural changes of surface roughness such as vegetation growth, γ_t is the transient coherence loss related to difference in soil moisture at the two acquisition times, and y_p is the permanent coherence loss related to sudden changes of surface roughness and micro-topography, i.e., soil erosion/deposition. γ_b follows an inverse logarithmic decay curve (e.g., in Australia: Castellazzi, 2021), with a progressive coherence decrease with image pairs of increasing temporal baselines (e.g., when using a single primary image stack design; Fig. 1C). γ_t is fully recoverable and depends on the transient nature of soil moisture anomalies. y_p is a permanent coherence loss, as surface soil structure and roughness changes are not time-dependant and are unrecoverable. Using an InSAR stacking approach, this study proposes to extract the contribution of γ_b by using selected pairs with similar temporal baselines, isolating coherence images with similar y_p signals from a stack and correcting for the temporally varying influence of γ_t via stacking.

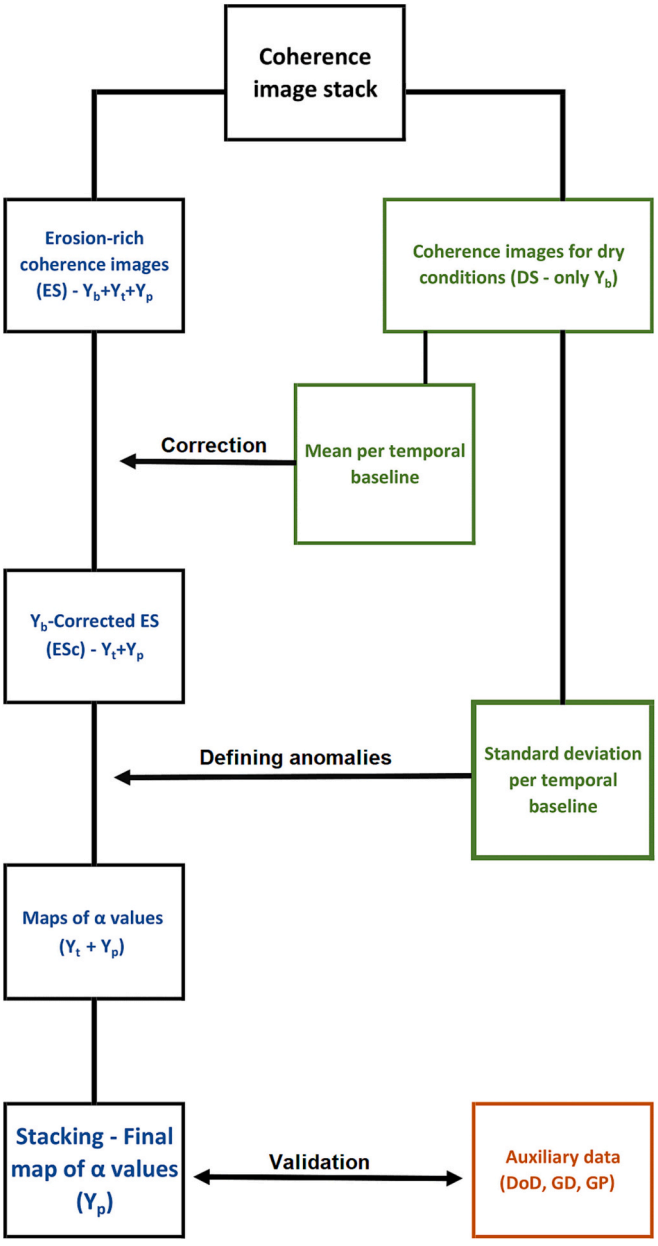

Fig. 5. Workflow presented in this study. Steps related to the Erosion-rich coherence (i.e., with high precipitation rates between the image pairs) images isolated from the stack are shown in blue, Steps related to the dry condition coherence are shown in green, and auxiliary data are shown in orange. (For interpretation of the references to colour in this figure legend, the reader is referred to the web version of this article.)

The approach divides the coherence stack into two sub-stacks: 1) an erosion-rich stack and 2) an erosion-poor stack (Fig. 5). The erosion-poor stack is used to correct the erosion-rich stack, removing the contribution of γ_b and isolating the contributions of γp and γt. Practically, the first step consists in selecting erosion-rich coherence images, creating an 'Erosion Sub-stack' (ES). The ES comprises all connections with dates encompassing a particular precipitation event. This stack is influenced by all three contributors γ_b, γ_t and γ_p. In the second step, a 'Dry Sub-stack' (DS) is identified by selecting all coherence images with no influence from rain events; it is assumed that this stack is only influenced by γ_b and γ_t. The DS corresponds to all 'dry conditions' coherence images, they are identified in the coherence stack using a criterion based on total precipitation before the first radar image acquisition and in between the two acquisitions. The criterion corresponds to a cumulative rain below 1% of the time-series maximum in the period starting 5 days prior to the first acquisition date and ending at the date of the last acquisition. It is important to note that for validation with auxiliary datasets measuring erosion between two dates, such as DoD data, the selection criterion for the ES stack is slightly modified: the ES is formed by a selection of coherence images between the two DoD dates which were not selected to form the DS.

The conversion from coherence images to maps of potential erosion hotspots follows two steps. First, all coherence images within an ES (i.e., a selection of coherence image containing erosion information) are corrected for γ_b by subtracting the average of all coherence maps with similar temporal baselines found within the DS. In other words, the average map calculated from all coherence images with N-days temporal baseline in the DS is subtracted to each coherence map with N-days temporal baseline in the ES. This strategy is applied to all temporal baselines found in the ES (all of the following: $N = 12$, 24, 36, 48 and 60-days). This step leads to a γ_b-corrected ES, referred to as ESc thereafter. Second, to define coherence loss anomalies, each coherence map in the ESc is divided by the standard deviation of all coherence maps with similar temporal baselines in the DS. This leads to the creation of coherence anomaly maps, expressed in a unitless term, referred to as 'α value' thereafter. Finally, an averaged coherence anomaly map is extracted by averaging all α-value maps. Averaging several observations aims at correcting for γ_t, the time-dependant component related to soil moisture changes.

4. Results and discussion

4.1. Identifying major precipitation events and dividing the coherence stacks

Prior to dividing the coherence image stack into sub-stacks, a characterisation of potential erosion-generating precipitation events is necessary. The daily precipitation time-series are used to constrain such analysis (Fig. 6 and S1 for Study area 2 and 1, respectively). We note that a major, 7-day precipitation event occurred in February 2019 in the

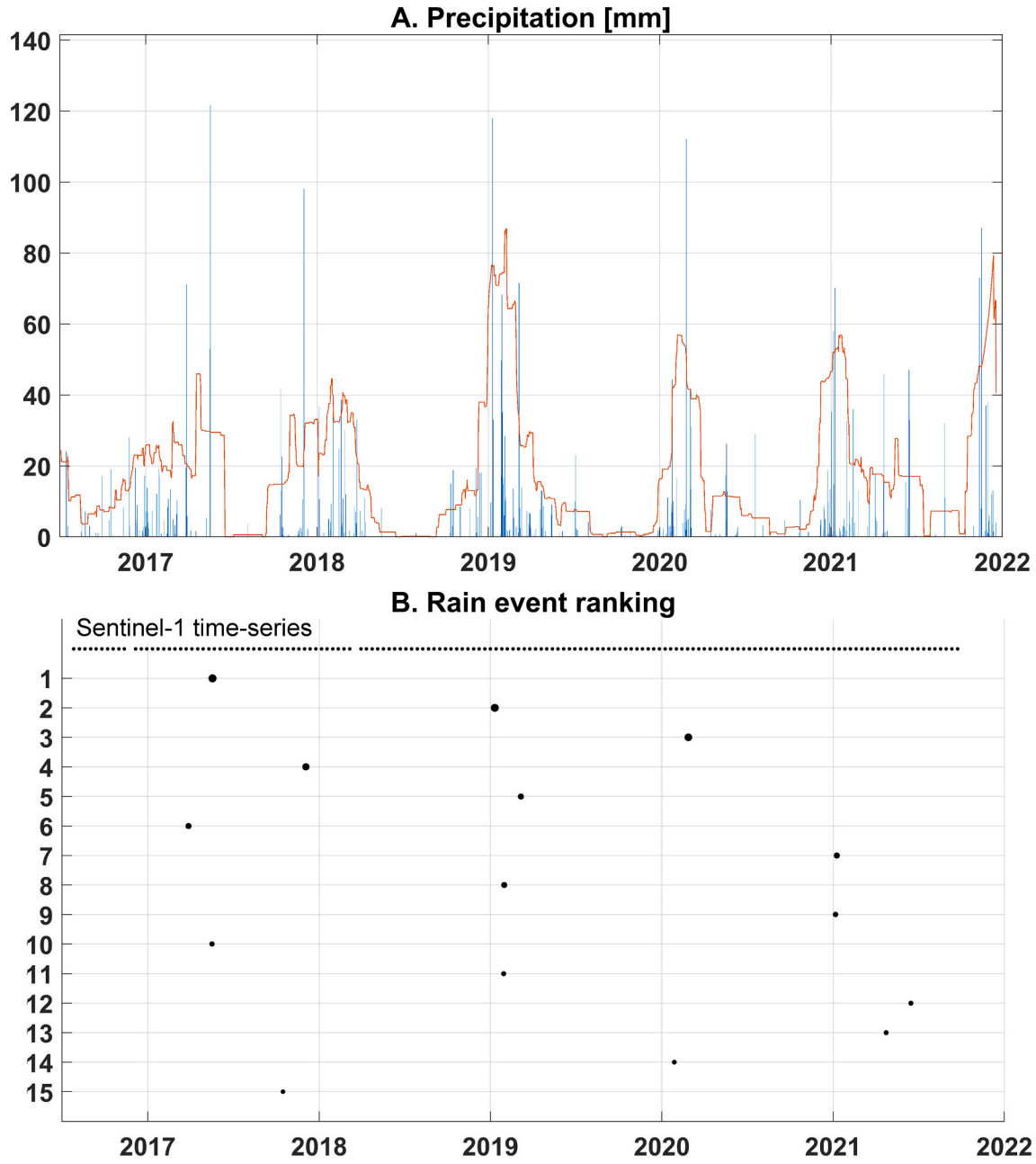

Fig. 6. Precipitation time-series (A) and ranking of precipitation days (B) for study area 2. An envelope curve (orange line) based on a 31-days moving mean is used to highlight seasonal patterns of precipitation (A).

study area 1 (Fig. S1) and corresponds to the seven most rainy days during the study period. The 8th and the 9th most rainy days occurred at different times, in early 2021 and in mid-2017, respectively.

4.2. Selection of radar image pairs

Based on the precipitation rates between and before each radar image pairs, the coherence pairs are classified into four sub-stacks (Fig. 7 for the study area 2; Fig. S2 for the study area 1). The number of connections per stack and the precipitation rates occurring between images forming each pair are presented in Table 4. In total 80 and 117 'dry pairs' were selected for study area 1 and 2, respectively, to form the dry stacks (DS). Such image pairs are expected to be erosion-free and to provide an accurate representation of the background coherence (γ_b) and its variability, both useful for correcting coherence images containing erosion information.

The number of dry connections is related to the total number of connections, the climate of the study area, and the criterion used to identify connections as dry. On the other hand, the number of connections for each major rain event sub-stacks are solely related to the density of the graph. With a maximum temporal baseline of 60 days, 15 connections were found to temporally intercept each rain event. They contain similar erosion information (γ_p) and varying moisture information (γ_t). Such connection graph design guarantees an efficient

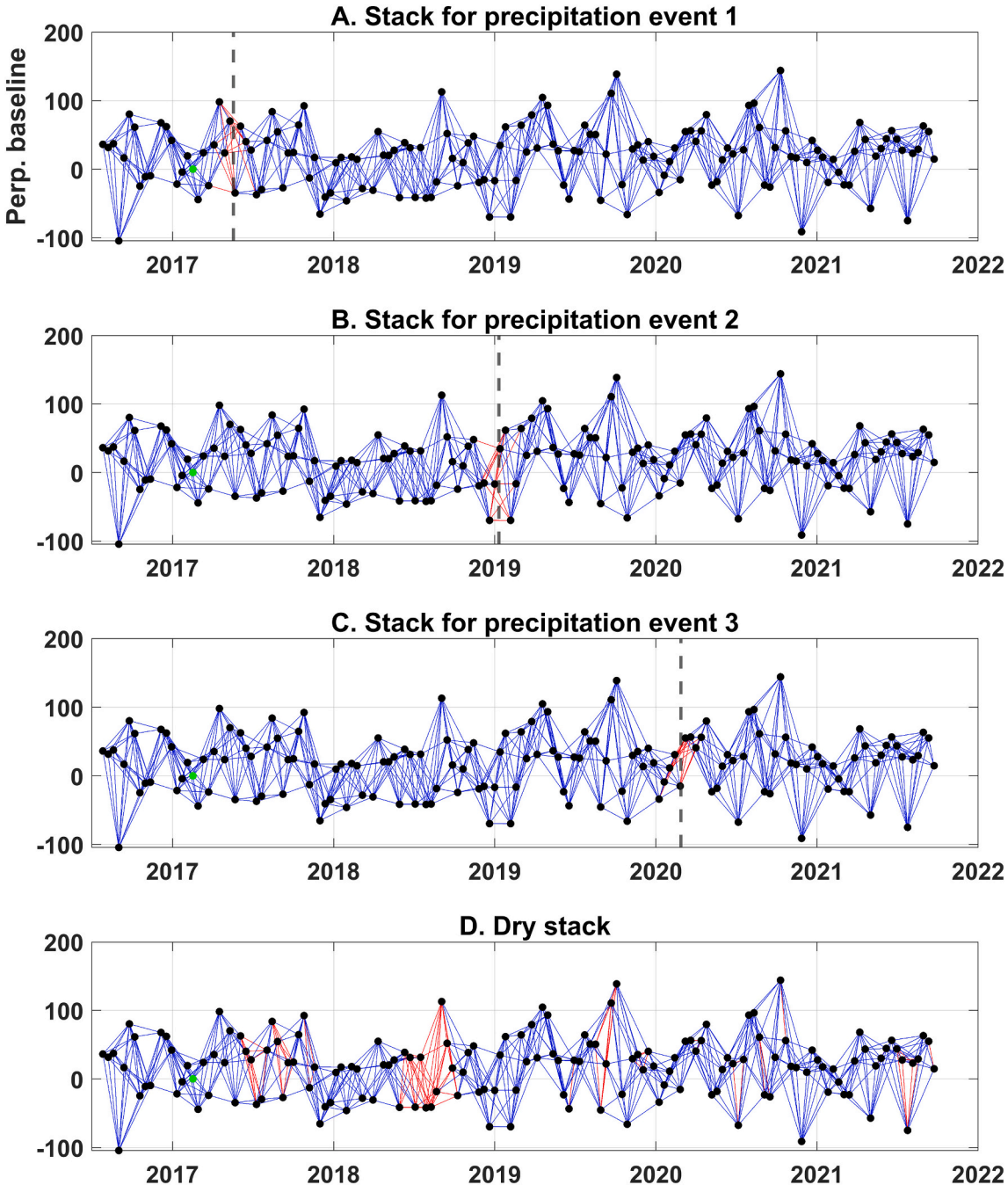

Fig. 7. Connection graph subsets for study area 2. Black dots represent radar acquisitions positioned on the time vs. perpendicular baseline plot, blue lines represent possible InSAR coherence pairs within the criteria (maximum temporal and perpendicular baselines), red lines represent selected pairs for each stack. (For interpretation of the references to colour in this figure legend, the reader is referred to the web version of this article.)

Table 4
Characteristics of the stack subsets for the two study areas. The difference in total precipitation between coherence pairs of the DS and the three ES guarantees the contrast in their erosion information content required for the CCD approach to be efficient.

Stack	Precipitation of the rainiest day in the stack (mm)	Precipitation between the coherence pairs [range] – mean (in mm)	Number of coherence maps
Study area 1 (Fig. 2C; Fig. 4)			
Dry stack	NA	[0–2] - 0.40	80
Stack for rain event 1	225	[977–1416] - 1229	15
Stack for rain event 2	91	[148–216] - 159	15
Stack for rain event 3	83	[276–550] - 401	15
Study area 2 (Fig. 2D; Fig. 5)			
Dry stack	NA	[0–1.1] – 0.19	117
Stack for rain event 1	122	[175–280] - 186	15
Stack for rain event 2	118	[161–468] - 291	15
Stack for rain event 3	112	[212–347] - 253	15

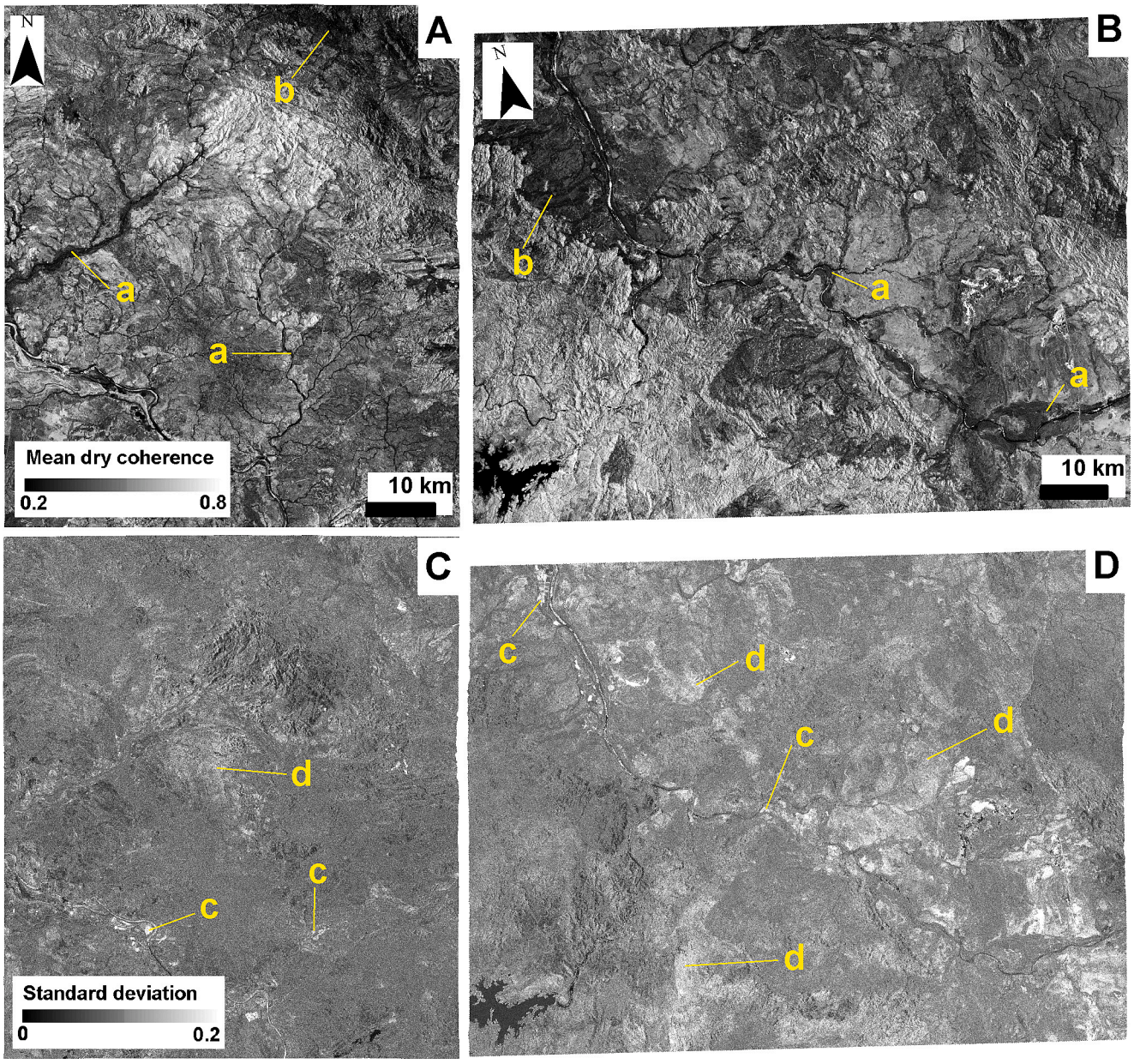

Fig. 8. Mean (A, B) and standard deviation (C, D) of the dry stack coherence for 12 days of temporal baseline and for study area 1 (A, C) and 2 (B, D). These maps (along with the ones for baselines of 24, 36, 48 and 60 days) are used to correct the background coherence component of pairs containing erosion information and to define anomalies beyond the coherence variations observed in dry conditions. (a) riparian vegetation; (b) permanent, dense vegetation; (c) zones of coherence variation around river corridors potentially due to temporary flooding; (d) areas of varying vegetation cover/density.

removal of any intermittent coherence loss (γ_t) due to moisture changes via averaging/stacking.

Coherence pairs in the DS intercept, on average, 1490 and 1280 times less rain than the erosion sub-stacks. This contrast is an important consideration as the DS is used to subtract γ_b but should not contain γ_p. In addition, as noted in the previous section, the identification of coherence connections is based on daily rain rates. Thus, the mean precipitation rates for coherence pairs within each ES do not align with the highest daily rain rates. Certain rain events span multiple days. Thus, while the maximum daily rain rate may not be the highest along the time-series, the total amount of rain between coherence pairs may still be high. This is observed, for example, for the rain Event 2 of the Study area 2, which has a high average rainfall per connection in comparison to the rain Event 1 for the same study area (Table 4).

4.3. Coherence of the dry stacks (DS)

The mean and standard deviation of the dry coherence stacks are the two statistical parameters used to 1) extract the y_b component of coherence from all coherence pairs within the ES and 2) set the threshold for identification of y_t and y_p anomalies (Fig. 5). These two parameters are calculated for each temporal baseline configuration of the stacks: 12, 24, 36, 48 and 60 days. Fig. 8 presents the two parameters for the temporal baseline of 12 days and for both study areas.

Low coherence and/or high standard deviation inherently suggest a local decrease of sensitivity in the final erosion products. First, the radar signal needs to be sufficiently coherent to be impacted by potential erosion and for the erosion-related coherence loss to be identifiable. Second, because the temporal variations of coherence without influence of erosion increases the threshold allowing to discriminate sudden non-recoverable erosion changes from seasonal variability of the background coherence response and potentially, from seasonal moisture changes. In other words, it acts as noise which masks the erosion signal in our workflow.

Observing Fig. 8, we note that corridors of vegetation such as riparian zones are showing low coherence values due to dense and permanent vegetation. Higher coherence variations are identified in places that are temporarily flooded in the DS, e.g., near rivers, during receding stream conditions after the rain season. It can also happen where a low and/or thick vegetation cover dies through the dry season, leading to temporally fluctuating coherence values.

Change of coherence in the DS due to temporal baseline change appears to be relatively slow and progressive (Fig. 9). Coherence loss is notably quicker in Study area 1, potentially due to the presence of low-lying vegetation. As expected, the 12-days coherence pairs are expected to be the most sensitive to erosion, with all coherence values between 0.2 and 0.8. Using longer temporal baseline pairs could potentially lead to a decrease of sensitivity but allow correcting for y_t via stacking. We note however, that the 60-days coherence pairs should remain sensitive to erosion, with most values remaining above 0.2.

4.4. Erosion-related anomalous coherence loss for major rain events

The coherence loss maps, expressed in proportion of the standard deviation of the erosion-free stack (unitless α-values), can be interpreted, after stacking multiple observations, as being related to soil surface changes. We note that the coherence in the ES is significantly smaller than in the DS (Fig. 10), with most values between 1 and −3 standard deviations of the DS (or α). By assuming that any erosion-free stack would vary positively and negatively in equal proportions in reference to the DS, we mirrored the positive part over the negative part (red bars in Fig. 10) to visually observe the anomalous coherence loss on the histogram. We conclude that for α-values of −1 or less, the coherence loss is potentially anomalous in reference to the DS.

It is important to note that stacking 15-images (Table 4) inherently reduce variance and narrows the histogram, explaining why positive values in the stacked-ES only barely reach +1 standard deviation of the un-stacked DS. We note that a proportion of that coherence loss might be

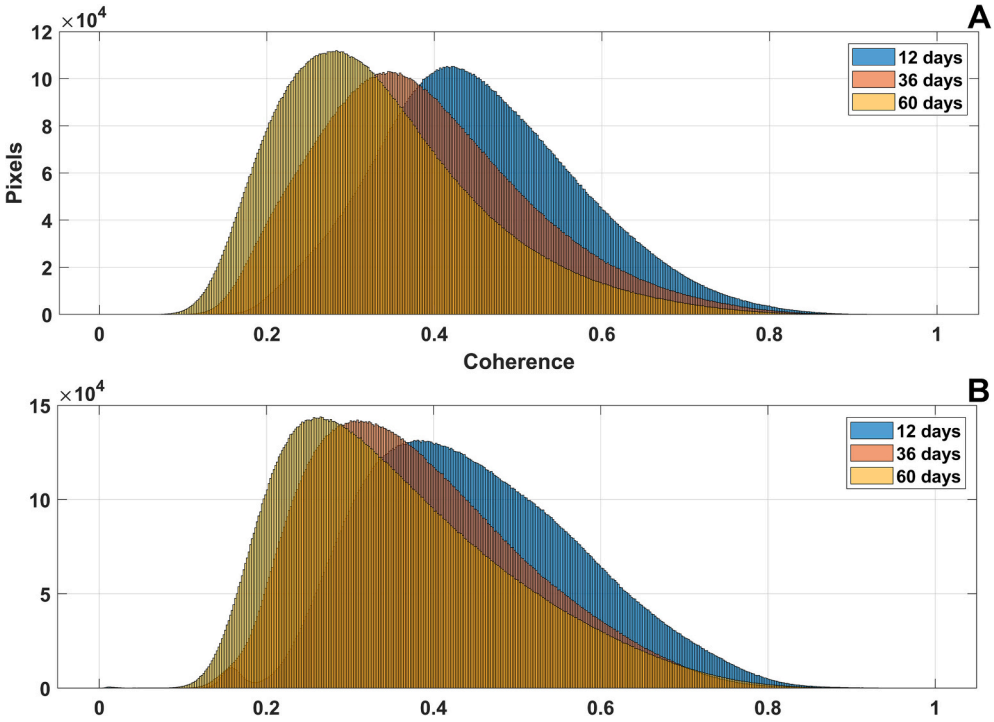

Fig. 9. Histograms of the background coherence images for study area 1 (A) and 2 (B) and for three temporal baselines. Histograms were produced after averaging all coherence images in the dry stacks.

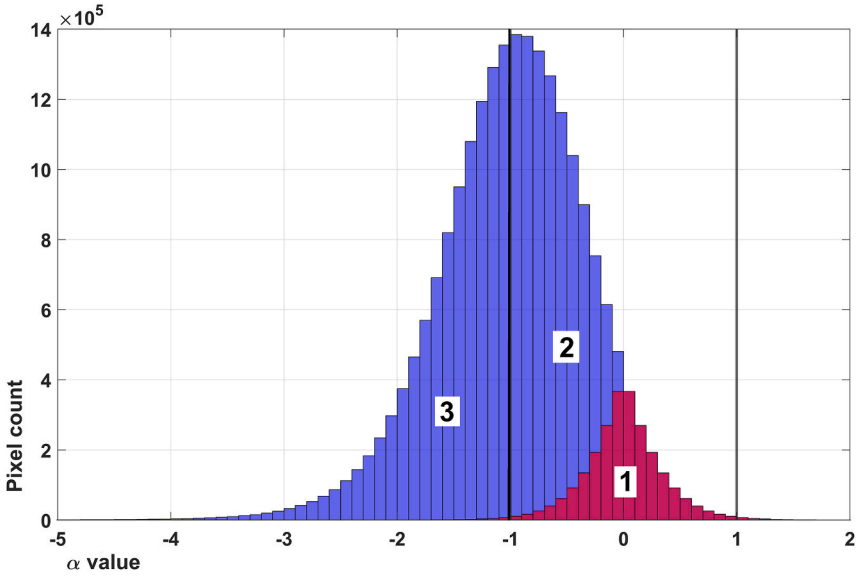

Fig. 10. Histogram of the final α values for the first rain event over study area 2, with visual interpretation of the anomalous coherence loss related to erosion vs. normal coherence variations. Part 1 represents the positive values of coherence loss and its corresponding (symmetrical) negative values, the positive values correspond to rare pixels for which coherence is higher in the ES than the DS; Part 2 represents coherence loss not attributable to erosion via a thresholding approach as it spreads across the same range as part 1; Part 3 represents the anomalous coherence loss attributable to erosion.

attributed to soil moisture changes potentially higher in the ES than in the DS. Attention will have to be paid to low-spatial frequency signals related to moisture residuals in the end-results. We also note that Fig. 10 presents a theoretical case, and that the threshold of interpretability of CCD maps will need to be verified with real-life test cases.

Anomalous coherence loss is detected for the three most important rain events occurred in study area 1 and 2 (Fig. 11). We note a general agreement for all three rain events and for both study areas. We also note the expected sensitivity loss along riparian corridors with typically dense and thick vegetation cover. For study area 2, a weaker coherence loss is observed for the first major rain event than for the two others (Fig. 11B). This agrees with the precipitation analysis (Table 4) which concluded than the highest daily rain rates do not coincide with the rain event with the highest total precipitation.

4.5. Gully-scale comparison with DoDs

DEMs of Difference (DoD) derived from 0.5 m resolution ALS DEMs (Aerial LiDAR Survey DEMs) were used to detect and measure erosion/deposition in the gullies in study area 2 (Table 3; see DoD locations on Fig. 4B; Khan et al., 2023). The CCD method described earlier was slightly modified for accurate comparison with DoDs, which aggregates the erosion information over a large temporal window. Instead of constraining the connection graph to a specific rain event (as for results presented previously, e.g., Fig. 11), 50 coherence images within the time window of the DoD are randomly selected to form the ES. Results can be interpreted as a mean coherence loss map free of any influence of soil moisture changes and reflecting the average, anomalous radar signal decorrelation due to soil surface changes for the time window of the DoD.

There were several inherent differences between radar CCD and DoDs, making their comparison challenging. First, they use different acquisition geometries (the angular acquisition geometry of the radar vs. a close-to-nadir laser detection). Second, their spatial resolution is different by at least one order of magnitude (tens of centimeters vs. tens of meters). Third, their time signature is different, as DoDs is a cumulative measurement between two dates of DEM acquisitions and CCD (in the case presented here) averages a set of individual measurements of radar signal decorrelation (corrected coherence maps) within a time-window. Fourth, their sensitivities are different. DoDs are sensitive to changes beyond a detection threshold in the order of tens of centimeters of elevation change. The exact sensitivity of InSAR CCD is largely unknown and depends on the radar wavelength. Two C-band radar images (e.g., Sentinel-1) will be completely decorrelated if the surface texture changes between the dates of acquisitions, even though the erosion rates are below DoD's detection threshold or if no change in elevation occurs.

In the large linear-alluvial Mount Wickham gully (length: 310 m and width: 150 m; Fig. 12A, B, C), both the DoD and the CCD detect major erosion near the boundary of the gully (Fig. 12B, C), particularly in the upper and mid sections of the gully (Fig. 12B – a,b). We note that coherence anomaly is detected solely where no vegetation occurs. Vegetation inside this gully might (Fig. 12A) have decreased the sensitivity of the CCD.

In the large alluvial Glen Bowen gully (length- 200 m and width 190 m; Fig. 12D, E, F), the DoD detected erosion within the gully channels rather than at the gully boundary (Fig. 12E, c) and the coherence loss was detected in wider mid/central regions of the gully as well (Fig. 12F). This is perhaps because while the DoD detects erosion above a certain level of detection threshold value (depending upon the precision of the DEM survey- ALS LiDAR in this case), it is unable to pick up subtle geomorphic changes such as sheetwash erosion and deposition that would lie within the level of detection threshold value. In contrast, coherence loss can detect spatial distribution of such subtle textural changes such as sheetwash erosion as well. However, CCD detection of erosion/deposition within the narrow gully channels is dependent on the radar line-of-sight (LOS) angle.

The linear Strathbogie gully (length- 320 m and width- 5 to 25 m; Fig. 12G, H, I) is relatively narrow compared to the large Mount Wickham and Glen Bowen gullies. Localised erosion is observed along the head cut and channel boundary during 2019–2021, as detected by DoD (Fig. 12H, d,e). The coherence method detected erosion in the widest sections of this gully but is unable to pick up changes in narrower cross-sections (Fig. 12I). This is potentially related to the limited penetration of the radar signal within the gully due to the LOS angle.

The results indicate that the CCD method is more efficient in wide, open, unvegetated, gullies where erosion is not restricted to narrow channels which cannot be penetrated/identified by the radar LOS angle. For example, we observe that the radar signal does not effectively penetrate the linear gullies at Strathbogie and hence is not capable of picking up the localised erosion in such narrow gullies. This also appears to be the case for incised channels within the Glen Bowen gully. In contrast, erosion/deposition appears well detected by CCD in a subset of

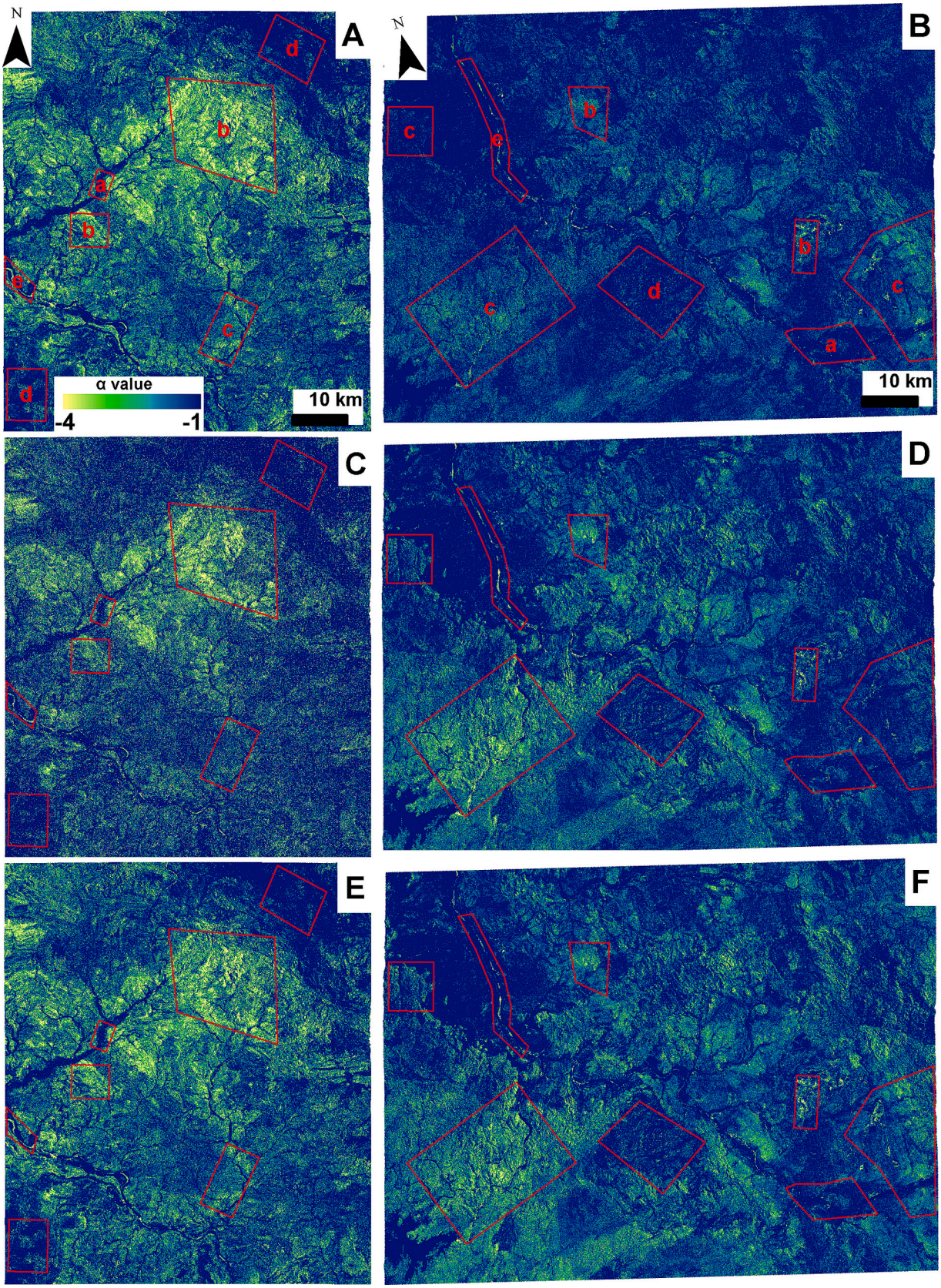

Fig. 11. Anomalous coherence loss (α value) calculated for the study area 1 (A, C, E) and 2 (B, D, F) and for the three first precipitation events identified on Fig. 6 and S1: events 1 (A, B), 2 (C, D) and 3 (E, F). Observations are highlighted as follow: examples of riparian vegetation interference (a), of areas with coherence loss for all rain events (b), of areas with varying degree of coherence loss (c), of areas of low coherence loss for all rain events (d), and of strong coherence loss along river channels (e).

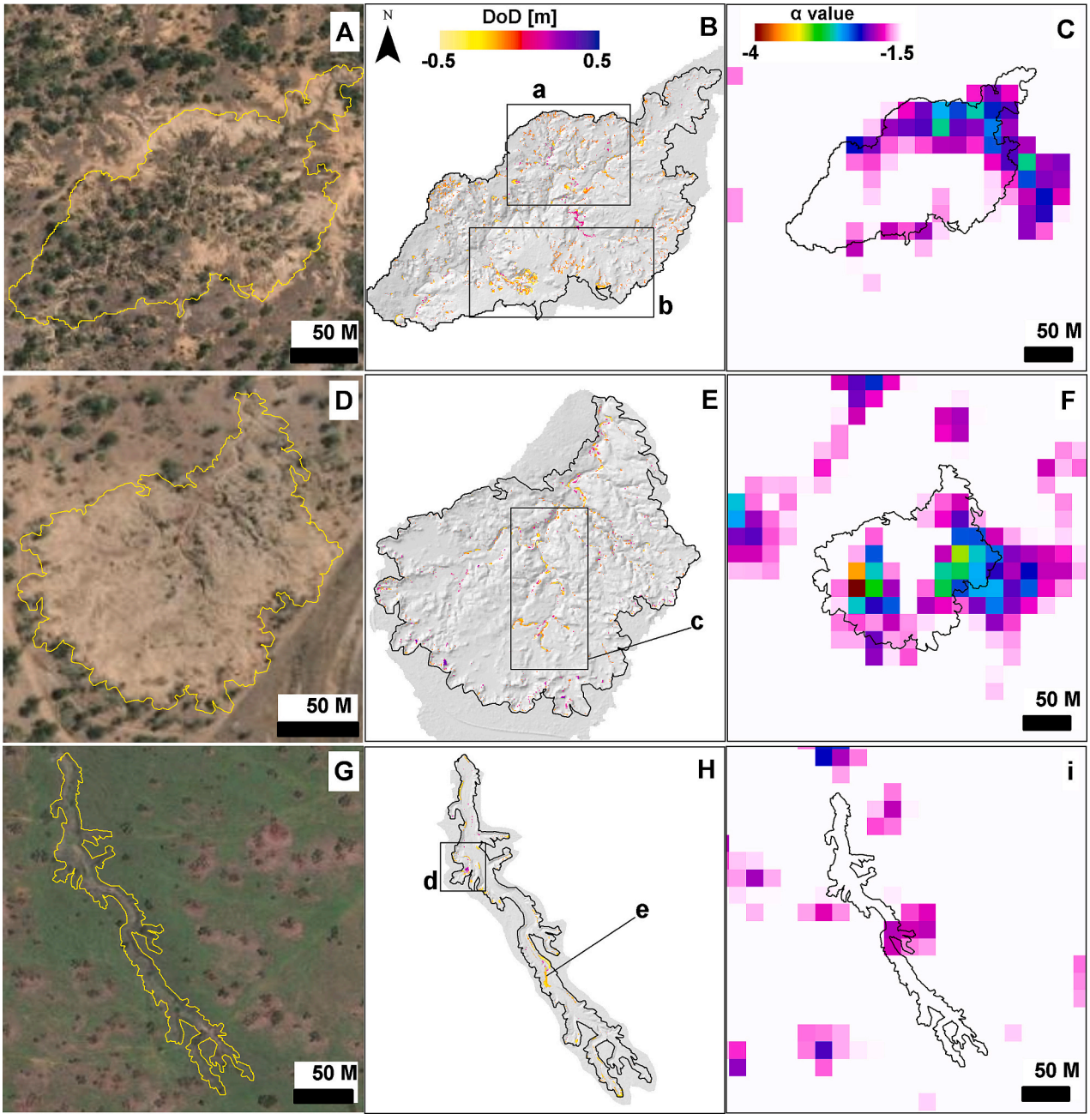

Fig. 12. Comparison between a colour-composite image (A,D,G), DoD data (B,E,H), and the anomalous coherence loss factor (α value) representative of the DoD temporal coverage for that site (C, F, I). A-C cover the Mount Wickham location, D-F cover the Glen Bowen location, and G-I cover the Strathbogie location (see Fig. 4 for locations). a,b,c,d and e highlights the main erosion features observable in DoDs. (Sources of colour-composite images: Esri, Maxar, GeoEye, Earthstar Geo-grpahics, CNES/Airbus DS, USDA, AeroGRID, IGN, and the GIS User community).

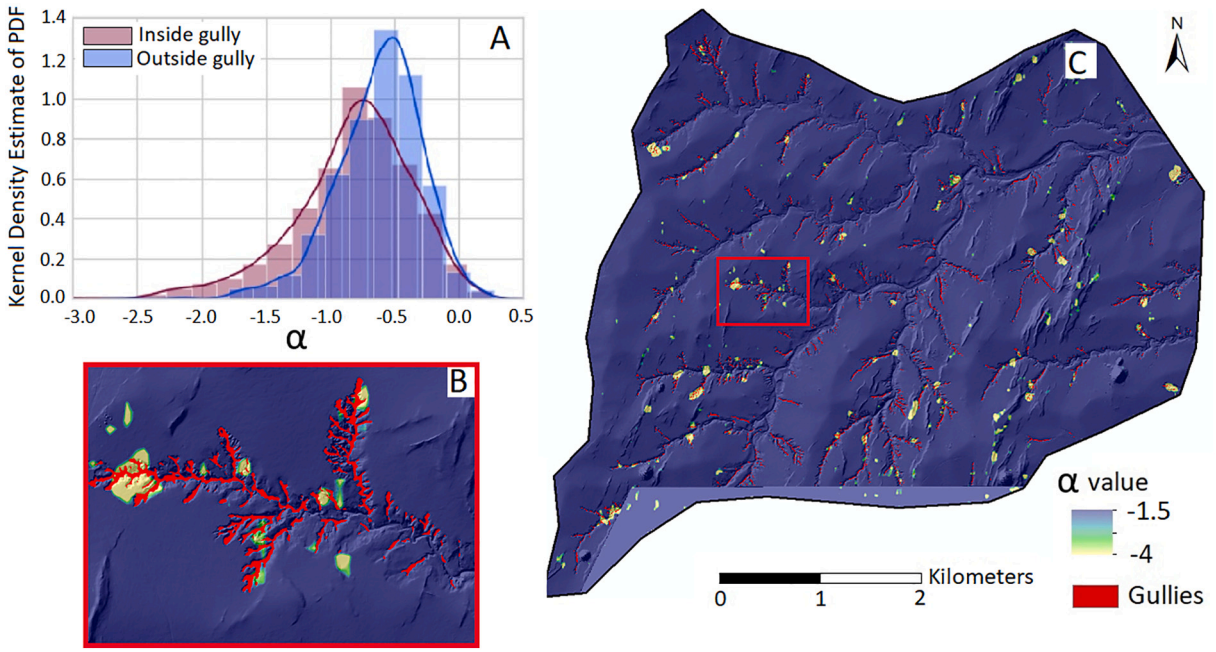

Fig. 13. Spatial coincidence between InSAR CCD maps and gully delineation (GD, Walker et al., 2020; overlaid as red contours) for Red Hill creek (Fig. 4B). A) shows a histogram of 10,000 random samples from gullied vs un-gullied cells; B) gives a fine-scale example of the spatial relationship between mapped gullies and InSAR-derived erosion; C) gives a broad-scale view of coincidence between gullies and InSAR-derived erosion. The InSAR data was resampled to a finer (1 m) resolution using bilinear interpolation to match the gully delineation data. PDF stands for Probability Density Function. (For interpretation of the references to colour in this figure legend, the reader is referred to the web version of this article.)

the floor area of large alluvial and linear-alluvial gullies. This emphasises the strength of detecting geomorphic change using complimentary change detection techniques - CCD and DoDs in this case. The occurrence of erosion within gullies is supported by a sediment source tracing study which indicated that denuded areas on hillslopes and within drainage areas such as gullies may collectively be sediment sources of comparable importance to vertical channel banks directly on waterways in the Bowen River catchment (Hancock et al., 2014; Daley et al., 2023).

4.6. Regional-scale comparison with gully maps

The CCD map calculated for the entire length of the InSAR stack for study area 2 (Table 1, Fig. 7) is compared with the gully delineation dataset from Walker et al. (2020, 2022) (Fig. 13). Gullies are delineated using the geometric criteria of landform elements with steep walls and flat floors existing at locally low elevation. These criteria are mapped using slope, profile curvature and landscape position across multiple scales. Anomalous coherence loss beyond -1α (or one standard deviation of a normal erosion-free coherence map) occurs preferentially within gullies, as highlighted by Fig. 13A. Low alpha values are also observed outside of gullies mapped in 2018 following the approach presented by Walker et al. (2020), potentially due to hillslope erosion, the creation of new gullies not identified by the gully delineation algorithm, or the expansion of delineated gullies. The latter is observed in Fig. 13B, where erosion that is possibly related to surface sheetwash or rilling around an identified gully is observed by CCD.

A comparison between CCD results and regional-scale gully delineation (Daley et al., 2021) is presented in Fig. 14. Two different thresholds are applied in maps (A) and (B), highlighting that most values in the range [−2 –1] occur outside of gullies. It also highlights the need to build expertise on interpretation of CCD maps for such applications. With few exceptions, values below -2α are only observed within gullies.

4.7. Regional-scale comparison with gullying potential maps

Overlaying the anomalous coherence loss maps calculated from the entire length of the InSAR stack to the gullying potential (GP) map proposed by Walker et al. (2020) provides interesting insights into the erosion activity of areas found to be at risk of gullying (Fig. 15). The coherence loss signal primarily occurs in the upslope portion of some zones at risk of gullying, suggesting that the early phases of sheetwash, rill and gully formation are occurring in these areas. Such behaviour is consistent with a sediment source tracing study in the Bowen River catchment which indicated that denuded areas on hillslopes and within drainage lines collectively may be sediment sources of comparable importance to vertical channel banks directly on waterways (Hancock et al., 2014). This application of InSAR takes advantage of the high sensitivity of the coherence loss mapping, where erosion rates might be low but textural change on the surface are sufficient to induce an observable loss of coherence. In addition, such observation is not challenged by the penetration of the InSAR signal into any specific topographic feature.

4.8. Complementarity between CCD, DoDs, and gullying potential maps

The three main pieces of erosion information presented in this paper (coherence loss maps, DoD, GP map) are presented for a specific gully channel over the Main Creek area (Fig. 16). A good correspondence is found between the CCD and the GP maps (Fig. 16A), with coherence loss observed above the gully head and spreading through a large section of the high GP values. The coherence loss signal is observed in the DoD within 50 m above the gully head (Fig. 16B), suggesting that the gully erodes not only at the headcut but erosion also progresses through surface degradation of the outer gully boundaries and along the GP channel (Fig. 16A).

Gully extension is typically driven by the hydrologic and topographic properties of the contributing drainage area upslope of the gully head (e.

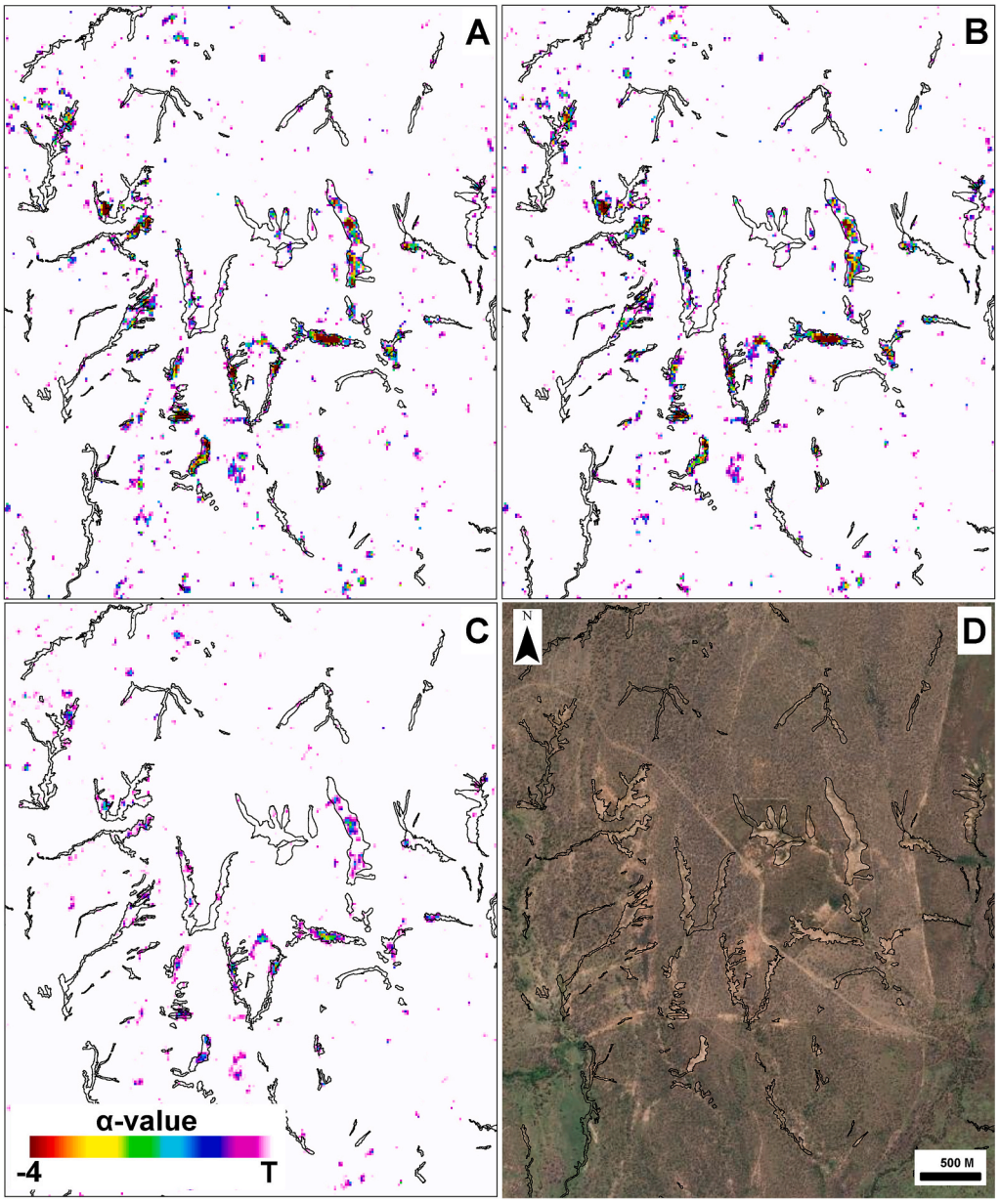

Fig. 14. Comparison between different α-value maps with regional-scale gully delineation from Daley et al., 2021 over the Collinsville area (Fig. 4). Three α-value maps are presented: for the most important rain event (A), for the three most important rain events (B) and a map based on an ensemble for the entire time-series (50 coherence maps not selected in the dry stack - C). As A and B aggregate erosion-affected coherence maps, thresholds (T) were adapted: −2 is used in A and B, and − 1.5 is used in C. The correspondence between α-values and gullies is obvious in all cases (A, B, C). A colour-composite image is presented in D for comparison (sources: Esri, Maxar, GeoEye, Earthstar Geogrpahics, CNES/Airbus DS, USDA, AeroGRID, IGN, and the GIS User community).

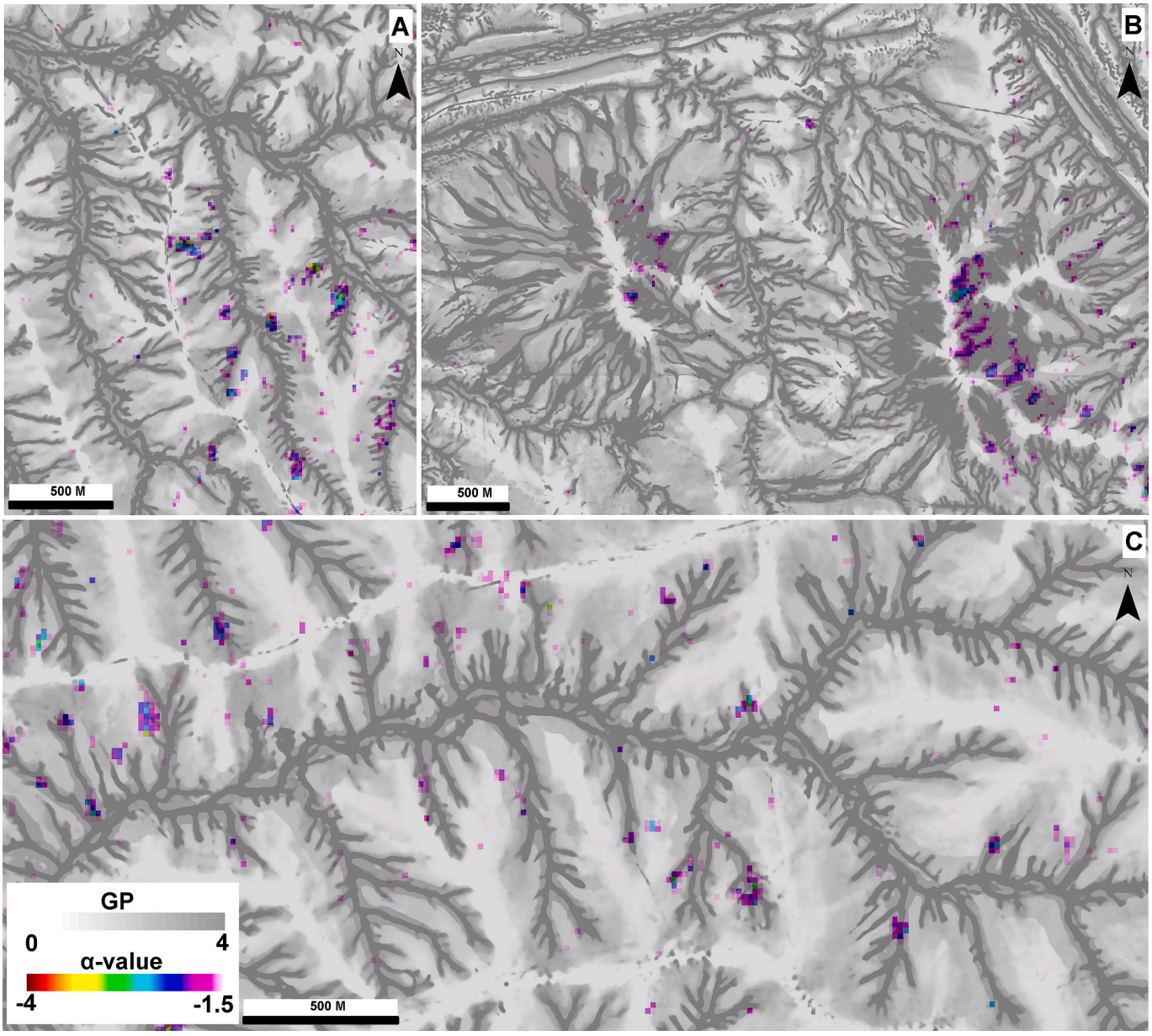

Fig. 15. Example of gullying potential (GP) maps (Walker et al., 2020) overlaid on the radar-derived α-values over (A) Weany Creek 1, (B) Bogie and (C) Weany Creek 2. Locations are presented on Fig. 4. The LiDAR data from which the gullying potential map is derived was acquired on August 8th, 2021; the InSAR-derived erosion map aggregates anomalous coherence loss data over the entire period of each InSAR stacks, i.e., August 2016 to September 2021 (Table 1). While α-values below −1.5 are shown here, the optimum threshold for interpretability is not known.

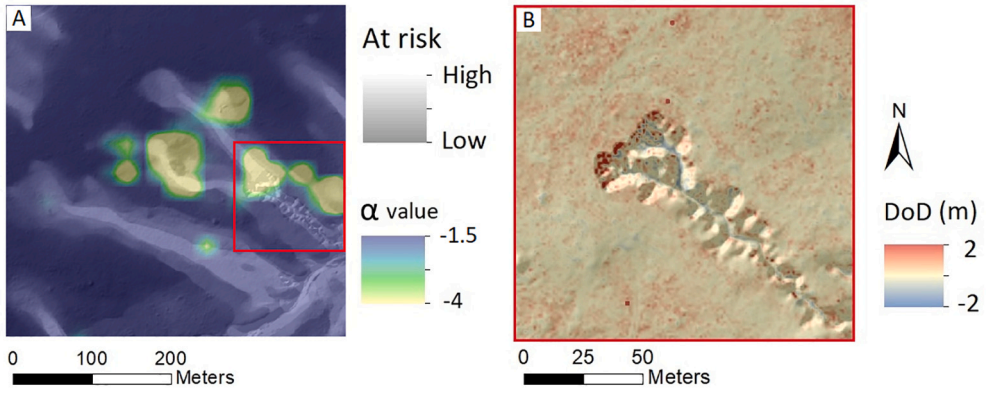

Fig. 16. Comparison between GP map (Walker et al., 2020) and InSAR (left) and DoD data (right) over a gully in the Main creek area (Fig. 4). The DoD was calculated as the difference in elevation between 2013 and 2021 with positive (red) values indicating erosion and negative (blue) values indicating deposition. (For interpretation of the references to colour in this figure legend, the reader is referred to the web version of this article.)

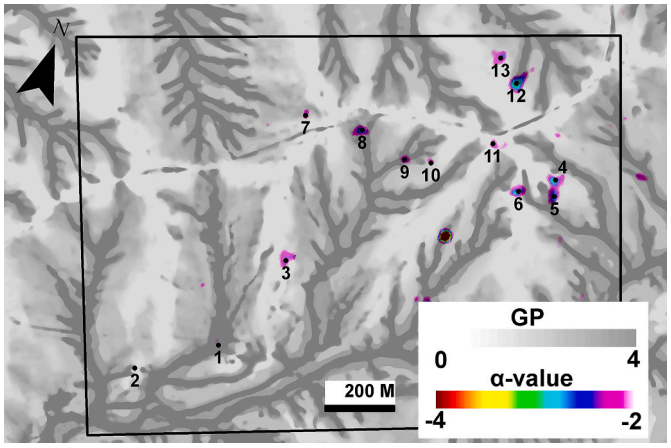

Fig. 17. Location of in situ sites and position on the GP and α-value maps.

g., Gómez-Gutiérrez et al., 2015; Vanmaercke et al., 2016). Hydrological indices such as stream power and topographic wetness index are often used to represent the susceptibility of a hillslope to gully erosion (e.g., Conoscenti and Rotigliano, 2020), as is used in the GP maps in Figs. 15 and 16. Stream power index is correlated with high sediment transport capacity (Prosser and Rustomji, 2000). The degree to which these indices predict gully erosion depends on local physiographic variables such as vegetation cover, soil type and rock fragment cover (Torri and Poesen, 2014). As a gully head advances upslope its contributing area also progressively decreases, leading to eventual hydraulic exhaustion (e.g., Torri and Poesen, 2014). The goal of most gully management strategies, such as revegetation of hillslopes, is to decrease concentrated flow into and increase the erosion resistance of the gully head to stabilise the gully (Valentin et al., 2005; Bartley et al., 2020). We show that combining CCD maps, DEMs of Difference (DoD) and gullying potential (GP) maps enables identification of actively eroding gullies with high potential for further incision (Fig. 15). The DoD confirms that the gully head is actively retreating upslope (Fig. 16B), while the GP map shows where the gully catchment area is susceptible to channel erosion before the gully approaches hydraulic exhaustion. The coherence loss map also indicates that active surface erosion is occurring within the area mapped to be at risk of channel incision and in subsets of the floor area of broad alluvial gullies (Daley et al., 2023). For site-scale gully management it is important to have a framework for identifying specific gullies as candidates for remediation. Through this example we have demonstrated that such a framework is possible by combining the three core analysis methods presented in this paper (CCD, DoDs and GP maps).

4.9. In situ verification of coherence loss anomalies

For verification of the coherence loss anomalies detected in the resultant InSAR output, field validation was conducted in November 2022. This timing was selected as this coincides with the end of the dry season/initiation of the wet season, when vegetation cover is low, and erosion/deposition might be easily seen. Several point locations were identified in the Weany Creek (within Study area 1) using the mean coherence loss map and the GP map from Walker et al. (2020). Among the selected points, based on site accessibility and weather conditions, 13 locations were surveyed (Fig. 17) focusing on identifying visible signs of soil erosion and/or deposition, recent surface changes from anthropogenic activities (cattle movement, road work), and recent land cover changes (Table 5). Field validation is expected to shed light on the validity of the method, including the occurrence of false-positive when the method is used for erosion mapping, which might include deposition or any type of other ground surface roughness changes temporally coinciding with wet periods, with or without causal relation with precipitation. Another expected output of field validation is (1) the thresholding of the α-value maps, to understand the level over which the coherence loss can be interpreted and (2) the complementarity between the α-value map and GP mapping.

All surveyed locations showed α-values below −2. This means that wet-period coherence values are decreased, in comparison to dry-period coherence, by at least 2 standard deviations of the dry-period coherence. Among the 13 surveyed points (Fig. 17), 6 showed obvious signs of erosion (examples presented in Fig. 18), 4 showed signs of frequent cattle circulation (Fig. 18D), and one was in close proximity to several active gully heads. No explanation could be drawn for 3 out of the 13 sites (sites 3, 5, 7), highlighting the need to further develop expertise in CCD map interpretation. For points with GP above 3, 3 out of 4 sites showed obvious signs of recent surface changes and potentially erosion (sites 1, 9, 12), confirming that the combination with a GP map might support interpretation of CCD maps by ruling out false positives observed over flat terrain (e.g., related cattle movements). When considering α-values below –2.5, surface roughness changes could be seen or inferred (e.g., observation of cattle tracks) in 6 out of 7 sites (4, 6, 8, 11, 12, 13), highlighting the potential to ease interpretation of CCD maps by thresholding in the range [−2.5–2]α. In addition, we note that (1) anthropogenic activities could lead to coherence loss signal in 4 out of 10 sites where surface roughness changes could be observed and (2) a potential signal leakage due to proximity of gully head is observed at one location (site 3), potentially related to the kernel integration inherent to InSAR coherence (in this case 5x5 pixels).

Table 5
Field observations in 12 locations shown on Fig. 17.

Location (Fig. 17)	Picture (Fig. 18)	α value	GP	Visible erosion or deposition	Visible anthropogenic disturbances	Landform/vegetation cover and potential changes
1	A	−2.03	3.96	X		Bare ground – surface changes likely
2		−2.11	2.01	X		Bare ground – surface changes likely
3		−2.43	1.23			No obvious changes – Proximity of gully head
4	B	−2.93	1.12	X		Bare soil – signs of erosion and surface changes
5		−2.74	3.38			No sign of soil changes – low, non-permanent vegetation
6		−2.70	1.88		Cattle	Nothing obvious except dead shrub
7		−2.33	2.38			Nothing obvious except dead shrub
8		−2.71	2.70		Cattle	Stable bedrock outcrop, nothing obvious except dead shrub
9	C	−2.37	4.92	X		Sandy gully, low lying vegetation
10	D	−2.28	1.57		Cattle	Mix of bare soil and deciduous vegetation
11		−2.54	1.56		Cattle	Mix of bare soil and deciduous vegetation
12	E	−3.12	3.97	X		Drainage lines, Bare soil with signs of surface changes
13	F	−2.54	1.07	X		Bare soil with signs of surface changes and dead vegetation

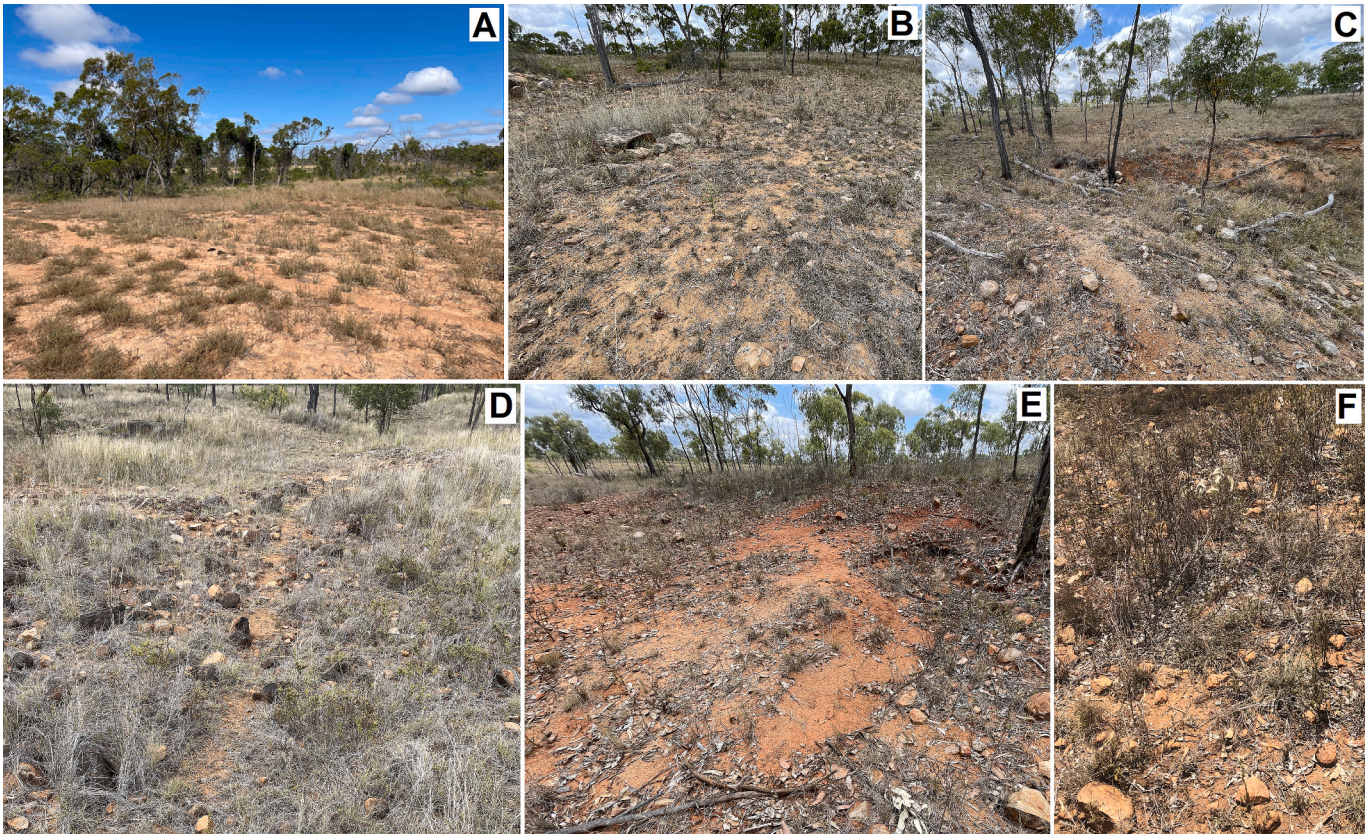

Fig. 18. Field observations on site 2 (A), 4 (B), 9 (C), 10 (D), 12 (E) and 13 (F). Bare ground and potential signs of recent surface changes can be seen in all pictures. Gullying is seen on (C), cattle tracks is seen on (D),

5. Conclusions and perspectives

By characterising the temporal decorrelation of the radar signal through InSAR Coherence Change Detection (CCD), it is possible to detect areas of surface changes, and to extract erosion information within erosion-affected coherence maps. The recent availability of large Sentinel-1 IW data time-series allows separation of such signal at temporal scales ranging from a single rain event to several years. The temporal density of these images allows applying a stacking approach leading to erosion maps free of artefacts from soil moisture and vegetation.

This paper proposes and tests a strategy to effectively extract the geomorphic change information from an SBAS-InSAR coherence image stack. The background coherence decay is characterised via observations drawn from 'dry coherence connections' not affected by erosion or deposition. The corrected stack contains sufficient data to smooth the transient component of coherence related to moisture changes. The resulting map is expressed in units of standard deviation of the erosion-free coherence variations, allowing to easily identify coherence loss anomalies and account for spatially varying noise levels related to vegetation.

Comparison with auxiliary datasets based on LiDAR survey and field observation indicates some of the benefits and limitations of the approach. The coherence analysis is particularly sensitive to any texture and surface roughness changes of the ground surface, and thus, not all observed decorrelations can be interpreted as erosion and compared to e.g., multi-temporal LiDAR data. The radar line of sight angle and resolution also severely constrains detection of erosion in narrow topographic features such as narrow gully morphologies. The technique appears to be particularly effective for observing erosion of small magnitude associated with the early development of gullies or the progression of current gullies beyond their extent, and with surface erosion within the floor of broad gullies, as this takes advantage of the high sensitivity of the coherence loss mapping over relatively flat terrain. Therefore, we conclude that C-band InSAR CCD is a complementary approach to airborne LiDAR for broad-scale mapping of erosion associated with gullies. Due to this complementarity, DEM of difference analysis informed how to interpret InSAR CCD erosion patterns but proved not to be suitable for directly testing them, hence they should be further tested by other means. Another benefit of coherence-based erosion mapping is the cost-effectiveness for large-scale applications. It is particularly suited to prioritising areas for land and grazing management, to prevent further gully expansion. It may also be useful to support the prioritisation of gully remediation projects, and in helping differentiate between active, inactive and potential gully erosion.

Future research includes (1) exploring the potential for long-wavelength, L-band InSAR CCD to map high erosion rates inside existing gullies and complement the observation of early gully development based on C-band data shown in this paper and (2) improving the extraction of the erosion information from a stack of anomalous coherence loss maps corrected for background coherence (γ_b). This includes testing data-driven methods to separate the erosion information and decompose mixed erosion signals, i.e., erosion of a specific rain event from erosion related to secondary events embedded in some of the CCD maps, particularly in coherence pair with longer temporal baselines. Finally, (3) testing different orbital direction and opposite LOS geometry could improve erosion mapping for deep gullies and stream banks. Such application should be tested where dense image time-series from both ascending and descending tracks are available, which, in Australia, is currently only possible in certain locations. Future availability of L-band NiSAR data will likely improve the capability of InSAR CCD to monitor sediment sources in rangelands and tropical savannas.

Supplementary data to this article can be found online at https://doi.org/10.1016/j.rse.2023.113546.

CRediT authorship contribution statement

Pascal Castellazzi: Conceptualization, Methodology, Software, Writing – original draft, Writing – review & editing, Formal analysis. **Sana Khan:** Validation, Formal analysis, Writing – review & editing. **Simon J. Walker:** Validation, Writing – review & editing, Formal analysis. **Rebecca Bartley:** Writing – review & editing, Supervision. **Scott N. Wilkinson:** Validation, Writing – review & editing, Supervision. **Jonathan C.L. Normand:** Writing – review & editing, Methodology.

Declaration of Competing Interest

The authors declare that they have no known competing financial interests or personal relationships that could have appeared to influence the work reported in this paper.

Data availability

All data sources are listed and publicly accessible

Acknowledgments

We acknowledge the European Space Agency (ESA) for acquiring and making available Sentinel-1 IW data. We thank the SARMAP team for their help and their efforts in continuously improving the SARSCAPE InSAR processing toolbox. We also thank the Australian Government's Reef Trust 3D Terrain Mapping Services Project (SON2615371) and Department of Defence for providing Lidar data. We gratefully acknowledge funding from CSIRO's Deep Earth Imaging Future Science Platform, the Australian Government's National Environmental Science Program (NESP) Tropical Water Quality Hub projects (Projects 2.1.4 and 5.9), the Queensland Government's Landholders Driving Change Program (LRP17-003 and LME17-009), the Australian Government's Reef Trust and Great Barrier Reef Foundation Project Assessing gully and stream bank erosion risk with LiDAR. We also thank the property owners for allowing access to their properties and involvement in the projects. Finally, thank you to the editor and two anonymous reviewers for providing critical peer review of this paper.

References

Bainbridge, Z., Lewis, S., Bartley, R., Fabricius, K., Collier, C., Waterhouse, J., Garzon-Garcia, A., Robson, B., Burton, J., Wenger, A., Brodie, J., 2018. Fine sediment and particulate organic matter: a review and case study on ridge-to-reef transport, transformations, fates, and impacts on marine ecosystems. Mar. Pollut. Bull. 135, 1205–1220. https://doi.org/10.1016/j.marpolbul.2018.08.002.

Bainbridge, Z., Lewis, S., Stevens, T., Petus, C., Lazarus, E., Gorman, J., Smithers, S., 2021. Measuring sediment grain size across the catchment to reef continuum: improved methods and environmental insights. Mar. Pollut. Bull. 168, 112339 https://doi.org/10.1016/j.marpolbul.2021.112339.

Bartley, R., Bainbridge, Z.T., Lewis, S.E., Kroon, F.J., Wilkinson, S.N., Brodie, J.E., Silburn, D.M., 2014. Relating sediment impacts on coral reefs to watershed sources, processes and management: a review. Sci. Total Environ. 468–469C, 1138–1153. https://doi.org/10.1016/j.scitotenv.2013.09.030.

Bartley, R., Croke, J., Bainbridge, Z.T., Austin, J.M., Kuhnert, P.M., 2015. Combining contemporary and long-term erosion rates to target erosion hot-spots in the Great Barrier Reef, Australia. Anthropocene 10, 1–12. https://doi.org/10.1016/j.ancene.2015.08.002.

Bartley, R., Thompson, C., Croke, J., Pietsch, T., Baker, B., Hughes, K., Kinsey-Henderson, A., 2018. Insights into the history and timing of post-European land use disturbance on sedimentation rates in catchments draining to the Great Barrier Reef. Mar. Pollut. Bull. 131, 530–546. https://doi.org/10.1016/j.marpolbul.2018.04.070.

Bartley, R., Poesen, J., Wilkinson, S., Vanmaercke, M., 2020. A review of the magnitude and response times for sediment yield reductions following the rehabilitation of gullied landscapes, 45, pp. 3250–3279. https://doi.org/10.1002/esp.4963.

Berardino, P., Fornaro, G., Lanari, R., Sansosti, E., 2002. A new algorithm for surface deformation monitoring based on small baseline differential SAR interferograms. IEEE Trans. Geosci. Remote Sens. 40, 2375–2383. https://doi.org/10.1109/TGRS.2002.803792.

Bui, L.K., Featherstone, W.E., Filmer, M.S., 2020. Disruptive influences of residual noise, network configuration and data gaps on InSAR-derived land motion rates using the SBAS technique. Remote Sens. Environ. 247, 111941 https://doi.org/10.1016/j.rse.2020.111941.

Cabré, A., Remy, D., Aguilar, G., Carretier, S., Riquelme, R., 2020. Mapping rainstorm erosion associated with an individual storm from InSAR coherence loss validated by field evidence for the Atacama Desert. Earth Surf. Process. Landf. 45, 2091–2106. https://doi.org/10.1002/esp.4868.

Castellazzi, P., 2021. InSAR Coherence Over Regional Australia: Implications for Mapping Groundwater-Related Ground Deformation, 2021 IEEE International Geoscience and Remote Sensing Symposium IGARSS, pp. 6044–6047. https://doi.org/10.1016/j.ejrh.2021.100774.

Castellazzi, P., Schmid, W., 2021. Interpreting C-band InSAR ground deformation data for large-scale groundwater management in Australia. J. Hydrol. Reg. Stud. 34, 100774.

Conoscenti, C., Rotigliano, E.J.G., 2020. Predicting gully occurrence at watershed scale: Comparing topographic indices and multivariate statistical models, 359, 107123. https://doi.org/10.1016/j.geomorph.2020.107123.

Coulthard, T.J., Neal, J.C., Bates, P.D., Ramirez, J., de Almeida, G.A.M., Hancock, G.R., 2013. Integrating the LISFLOOD-FP 2D hydrodynamic model with the CAESAR model: implications for modelling landscape evolution. Earth Surf. Process. Landf. 38, 1897–1906. https://doi.org/10.1002/esp.3478.

Daley, J., Stout, J., Curwen, G., Brooks, A., Spencer, J., 2021. Development and application of automated tools for high resolution gully mapping and classification from lidar data. Report to the National Environmental Science Program. Reef and Rainforest Research Centre Limited, Cairns (169pp.).

Daley, J.S., Spencer, J.R., Brooks, A.P., Stout, J.C., Thwaites, R., 2023. Direct rain splash and downwearing of internal surfaces as an important erosion process in alluvial gully development. CATENA 221, 106760. https://doi.org/10.1016/j.catena.2022.106760.

Darr, S.D., Pringle, M.J., 2017. Improving gully density maps for modelling water quality within Great Barrier Reef Catchments. In: Syme, G., Hatton MacDonald, D., Fulton, B., Piantadosi, J. (Eds.), MODSIM2017, 22nd International Congress on Modelling and Simulation. Modelling and Simulation Society of Australia and New Zealand, Hobart, pp. 1920–1926.

Dietrich, W.E., Perron, J.T., 2006. The search for a topographic signature of life. Nature 439, 411–418. https://doi.org/10.1038/nature04452.

Dietrich, W.E., Bellugi, D.G., Sklar, L.S., Stock, J.D., Heimsath, A.M., Roering, J.J., 2013. Geomorphic transport laws for predicting landscape form and dynamics. In: Wilcock, P.R., Iverson, R.M. (Eds.), Geophysical Monograph Series. American Geophysical Union, Washington, D. C, pp. 103–132. https://doi.org/10.1029/135GM09.

Gómez-Gutiérrez, Á., Conoscenti, C., Angileri, S.E., Rotigliano, E., Schnabel, S.J.N.H., 2015. Using topographical attributes to evaluate gully erosion proneness (susceptibility) in two mediterranean basins. Adv. Limitat. 79, 291–314. https://doi.org/10.1007/s11069-015-1703-0.

Goodwin, N.R., Armston, J.D., Muir, J., Stiller, I., 2017. Monitoring gully change: a comparison of airborne and terrestrial laser scanning using a case study from Aratula, Queensland. Geomorphology 282, 195–208. https://doi.org/10.1016/j.geomorph.2017.01.001.

Hancock, G.J., Wilkinson, S.N., Hawdon, A.A., Keen, R.J., 2014. Use of fallout tracers ^{7}Be, ^{210}Pb and ^{137}Cs to distinguish the form of sub-surface soil erosion delivering sediment to rivers in large catchments, 28, pp. 3855–3874. https://doi.org/10.1002/hyp.9926.

Jarihani, B., Sidle, R.C., Bartley, R., Roth, C.H., Wilkinson, S.N., 2017. Characterisation of Hydrological Response to Rainfall at Multi Spatio-Temporal Scales in Savannas of Semi-Arid Australia, 9, p. 540. https://doi.org/10.3390/w9070540.

Jiang, C., Fan, W., Yu, N., Nan, Y., 2021. A New Method to Predict Gully Head Erosion in the Loess Plateau of China Based on SBAS-InSAR, 13, p. 421. https://doi.org/10.3390/rs13030421.

Jordan, T.E., Lohman, R.B., Tapia, L., Pfeiffer, M., Scott, C.P., Amundson, R., Godfrey, L., Riquelme, R., 2020. Surface materials and landforms as controls on InSAR permanent and transient responses to precipitation events in a hyperarid desert, Chile. Remote Sens. Environ. 237, 111544 https://doi.org/10.1016/j.rse.2019.111544.

Khan, S., Bartley, R., Kinsey-Henderson, A., Hawdon, A.A., 2023. Application of multi temporal Lidar DEMs for tracking gully rehabilitation efforts in highly erosive landscapes of the Burdekin catchment in Queensland, Australia. Geomorphology. https://doi.org/10.2139/ssrn.4086561.

Kim, J., Dorjsuren, M., Choi, Y., Purevjav, G., 2020. Reconstructed aeolian surface erosion in southern Mongolia by multi-temporal InSAR phase coherence analyses. Front. Earth Sci. 8 https://doi.org/10.3389/feart.2020.531104.

Kim, J.-R., Lin, C.-W., Lin, S.-Y., 2021. The use of InSAR phase coherence analyses for the monitoring of aeolian erosion. Remote Sens. 13, 2240. https://doi.org/10.3390/rs13122240.

Kinsey-Henderson, A., Hawdon, A., Bartley, R., Wilkinson, S.N., Lowe, T., 2021. Applying a hand-held laser scanner to monitoring gully Erosion: workflow and evaluation. Remote Sens. 13 (19), 4004. https://doi.org/10.3390/rs13194004.

Koci, J., Jarihani, B., Leon, J.X., Sidle, R.C., Wilkinson, S.N., Bartley, R., 2017. Assessment of UAV and ground-based structure from motion with multi-view stereo photogrammetry in a gullied savanna catchment. ISPRS Int. J. Geo Inf. 6 (11) https://doi.org/10.3390/ijgi6110328.

Koci, J., Wilkinson, S.N., Hawdon, A.A., Kinsey-Henderson, A.E., Bartley, R., Goodwin, N.R., 2021. Rehabilitation effects on gully sediment yields and vegetation in a savanna rangeland. Earth Surf. Process. Landf. 46 (5), 1007–1025. https://doi.org/10.1002/esp.5076.

Kondolf, G.M., 1997. PROFILE: hungry water: effects of dams and gravel mining on river channels. Environ. Manag. 21, 533–551. https://doi.org/10.1007/s002679900048.

Kondolf, G.M., Schmitt, R.J.P., Carling, P., Darby, S., Arias, M., Bizzi, S., Castelletti, A., Cochrane, T.A., Gibson, S., Kummu, M., Oeurng, C., Rubin, Z., Wild, T., 2018. Changing sediment budget of the Mekong: cumulative threats and management strategies for a large river basin. Sci. Total Environ. 625, 114–134. https://doi.org/10.1016/j.scitotenv.2017.11.361.

Kondolf, G.M., Schmitt, R.J.P., Carling, P.A., Goichot, M., Keskinen, M., Arias, M.E., Bizzi, S., Castelletti, A., Cochrane, T.A., Darby, S.E., Kummu, M., Minderhoud, P.S.J., Nguyen, D., Nguyen, H.T., Nguyen, N.T., Oeurng, C., Opperman, J., Rubin, Z., San, D.C., Schmeier, S., Wild, T., 2022. Save the Mekong Delta from drowning. Science 376, 583–585. https://doi.org/10.1126/science.abm5176.

Lefort, A., Grippa, M., Walker, N., Stewart, L.J., Woodhouse, I.H., 2004. Change detection across the Nasca pampa using spaceborne SAR interferometry. Int. J. Remote Sens. 25, 1799–1803. https://doi.org/10.1080/0143116031000117038.

Lewis, S.E., Bartley, R., Wilkinson, S.N., Bainbridge, Z.T., Henderson, A.E., James, C.S., Irvine, S.A., Brodie, J.E., 2021. Land use change in the river basins of the Great Barrier Reef, 1860 to 2019: a foundation for understanding environmental history across the catchment to reef continuum. Mar. Pollut. Bull. 166, 112193 https://doi.org/10.1016/j.marpolbul.2021.112193.

Liu, J., Lee, H., Pearson, T., 1999. Detection of rapid erosion in SE Spain using ERS SAR interferometric coherence imagery. SPIE. https://doi.org/10.1117/12.373131.

Liu, J.G., Black, A., Lee, H., Hanaizumi, H., Moore, J.M., 2001. Land surface change detection in a desert area in Algeria using multi-temporal ERS SAR coherence images. Int. J. Remote Sens. 22, 2463–2477. https://doi.org/10.1080/01431160119991.

Liu, J.G., Mason, P., Hilton, F., Lee, H., 2004. Detection of rapid erosion in SE Spain. Photogramm. Eng. Remote. Sens. 70, 1179–1185. https://doi.org/10.14358/PERS.70.10.1179.

Mariotti, A., Croke, J., Bartley, R., Kelley, S.E., Ward, J., Fülöp, R.-H., Rood, A.H., Rood, D.H., Codilean, A.T., Wilcken, K., Fifield, K., 2021. Pre-development denudation rates for the Great Barrier Reef catchments derived using 10Be. Mar. Pollut. Bull. 172, 112731 https://doi.org/10.1016/j.marpolbul.2021.112731.

McCloskey, G.L., Baheerathan, R., Dougall, C., Ellis, R., Bennett, F.R., Waters, D., Darr, S., Fentie, B., Hateley, L.R., Askildsen, M., 2021. Modelled estimates of fine sediment and particulate nutrients delivered from the Great Barrier Reef catchments. Mar. Pollut. Bull. 165, 112163 https://doi.org/10.1016/j.marpolbul.2021.112163.

Olen, S., Bookhagen, B., 2020. Applications of SAR Interferometric Coherence Time Series: Spatiotemporal Dynamics of Geomorphic Transitions in the South-Central Andes., 125 https://doi.org/10.1029/2019JF005141 e2019JF005141.

Parker, A.L., Castellazzi, P., Fuhrmann, T., Garthwaite, M.C., Featherstone, W.E., 2021a. Applications of Satellite Radar Imagery for Hazard Monitoring: Insights from Australia, 13, p. 1422. https://doi.org/10.3390/rs13081422.

Parker, A.L., Pigois, J.P., Filmer, M.S., Featherstone, W.E., Timms, N.E., Penna, N.T., 2021b. Land uplift linked to managed aquifer recharge in the Perth Basin, Australia. Int. J. Appl. Earth Obs. Geoinf. 105, 102637 https://doi.org/10.1016/j.jag.2021.102637.

Phillips, J.D., 2021. Observing landscape evolution. In: Landscape Evolution. Elsevier, pp. 69–95. https://doi.org/10.1016/B978-0-12-821725-2.00003-X.

Piégay, H., Arnaud, F., Belletti, B., Bertrand, M., Bizzi, S., Carbonneau, P., Dufour, S., Liébault, F., Ruiz-Villanueva, V., Slater, L., 2020. Remotely sensed rivers in the Anthropocene: state of the art and prospects. Earth Surf. Process. Landf. 45, 157–188. https://doi.org/10.1002/esp.4787.

Prosser, I.P., Rustomji, P., 2000. Sediment transport capacity relations for overland flow, 24, pp. 179–193. https://doi.org/10.1177/030913330002400202.

Qin, Y., Mueller, N.D., Siebert, S., Jackson, R.B., AghaKouchak, A., Zimmerman, J.B., Tong, D., Hong, C., Davis, S.J., 2019. Flexibility and intensity of global water use. Nat. Sustain. 2, 515–523. https://doi.org/10.1038/s41893-019-0294-2.

Roberts, D., Wilford, J., Ghattas, O., 2019. Exposed soil and mineral map of the Australian continent revealing the land at its barest. Nat. Commun. 10, 5297. https://doi.org/10.1038/s41467-019-13276-1.

Schepanski, K., Wright, T.J., Knippertz, P., 2012. Evidence for flash floods over deserts from loss of coherence in InSAR imagery, 117. https://doi.org/10.1029/2012JD017580.

Schmitt, R.J.P., Bizzi, S., Castelletti, A., 2016. Tracking multiple sediment cascades at the river network scale identifies controls and emerging patterns of sediment connectivity. Water Resour. Res. 52, 3941–3965. https://doi.org/10.1002/2015WR018097.

Schmitt, R.J.P., Bizzi, S., Castelletti, A.F., Kondolf, G.M., 2018. Stochastic modeling of sediment connectivity for reconstructing sand fluxes and origins in the unmonitored Se Kong, Se San, and Sre Pok tributaries of the Mekong River: stochastic connectivity modelling. J. Geophys. Res. Earth Surf. 123, 2–25. https://doi.org/10.1002/2016JF004105.

Scott, C.P., Lohman, R.B., Jordan, T.E., 2017. InSAR constraints on soil moisture evolution after the March 2015 extreme precipitation event in Chile. Scie. Rep. 7, 4903. https://doi.org/10.1038/s41598-017-05123-4.

Shellberg, J., Brooks, A., Spencer, J., 2010. Land-use change from indigenous management to cattle grazing initiates the gullying of alluvial soils in northern Australia. In: Proceedings of the 19th World Congress of Soil Science: Soil solutions for a changing world, Brisbane, Australia, 1-6 August 2010. Symposium 4.3.1 impacts of land use change in unsustainable ecosystems: 59-62.

Smith, L.C., Alsdorf, D.E., Magilligan, F.J., Gomez, B., Mertes, L.A.K., Smith, N.D., Garvin, J.B., 2000. Estimation of erosion, deposition, and net volumetric change caused by the 1996 Skeiðarársandur jökulhlaup, Iceland, from Synthetic Aperture Radar Interferometry. Water Resour. Res. 36, 1583–1594. https://doi.org/10.1029/1999WR900335.

Steffen, W., Richardson, K., Rockström, J., Cornell, S.E., Fetzer, I., Bennett, E.M., Biggs, R., Carpenter, S.R., de Vries, W., de Wit, C.A., Folke, C., Gerten, D., Heinke, J., Mace, G.M., Persson, L.M., Ramanathan, V., Reyers, B., Sörlin, S., 2015. Planetary boundaries: Guiding human development on a changing planet 347, 1259855. https://doi.org/10.1126/science.1259855.

Steffen, W., Rockström, J., Richardson, K., Lenton, T.M., Folke, C., Liverman, D., Summerhayes, C.P., Barnosky, A.D., Cornell, S.E., Crucifix, M., Donges, J.F., Fetzer, I., Lade, S.J., Scheffer, M., Winkelmann, R., Schellnhuber, H.J., 2018. Trajectories of the Earth System in the Anthropocene 115, 8252–8259. https://doi.org/10.1073/pnas.1810141115.

Summerfield, M.A., 2014. Global geomorphology. Routledge.

Takaku, J., Tadono, T., Doutsu, M., Ohgushi, F., Kai, H., 2020. Updates of `AW3D30' Alos Global Digital Surface Model with Other Open Access Datasets, 43B4, pp. 183–189. https://doi.org/10.5194/isprs-archives-XLIII-B4-2020-183-2020.

Tangi, M., Bizzi, S., Fryirs, K., Castelletti, A., 2022. A dynamic, network scale sediment (dis) connectivity model to reconstruct historical sediment transfer and river reach sediment budgets. Water Resour. Res. 58 https://doi.org/10.1029/2021WR030784.

Thwaites, R.N., Brooks, A.P., Pietsch, T.J., Spencer, J.R., 2022. What type of gully is that? The need for a classification of gullies. Earth Surf. Process. Landf. 47, 109–128. https://doi.org/10.1002/esp.5291.

Torri, D., Poesen, J., 2014. A review of topographic threshold conditions for gully head development in different environments. Earth Sci. Rev. 130, 73–85. https://doi.org/10.1016/j.earscirev.2013.12.006.

Valentin, C., Poesen, J., Li, Y.J.C., 2005. Gully erosion: impacts, factors and control. Catena 63 (2–3), 132–153. https://doi.org/10.1016/j.catena.2005.06.001.

Vanmaercke, M., Poesen, J., Van Mele, B., Demuzere, M., Bruynseels, A., Golosov, V., Bezerra, J.F.R., Bolysov, S., Dvinskih, A., Frankl, A.J.E.-S.R., 2016. How fast do gully headcuts retreat?, 154, pp. 336–355. https://doi.org/10.1016/j.earscirev.2016.01.009.

Vorosmarty, C.J., 2000. Global water resources: vulnerability from climate change and population growth. Science 289, 284–288. https://doi.org/10.1126/science.289.5477.284.

Vrieling, A., 2006. Satellite remote sensing for water erosion assessment: a review. CATENA 65, 2–18. https://doi.org/10.1016/j.catena.2005.10.005.

Walker, S.J., Wilkinson, S.N., van Dijk, A.I.J.M., Hairsine, P.B., 2020. A multi-resolution method to map and identify locations of future gully and channel incision. Geomorphology 358, 107115. https://doi.org/10.1016/j.geomorph.2020.107115.

Walker, S., Wilkinson, S., Levick, S., 2022. Metre-resolution gully and erosion hazard mapping from airborne LiDAR in catchments of the Great Barrier Reef. CSIRO. https://doi.org/10.25919/7dsj-2r16.

Waterhouse, J., Schaffelke, B., Bartley, R., Eberhard, R., Brodie, J., Star, M., Thorburn, P. J., Rolfe, J., Ronan, M., Taylor, B., Kroon, F., 2017. Scientific Consensus Statement: Land Use Impacts on Great Barrier Reef Water Quality and Ecosystem Condition. Queensland Government.

Wegmuller, U., Strozzi, T., Farr, T., Werner, C.L., 2000. Arid land surface characterization with repeat-pass SAR interferometry. IEEE Trans. Geosci. Remote Sens. 38, 776–781. https://doi.org/10.1109/36.842006.

Wilkinson, S.N., Hancock, G.J., Bartley, R., Hawdon, A.A., Keen, R., 2013. Using sediment tracing to assess processes and spatial patterns of erosion in grazed rangelands, Burdekin River basin, Queensland, Australia. Agric. Ecosyst. Environ. 180, 90–102. https://doi.org/10.1016/j.agee.2012.02.002.

Wilkinson, S.N., Kinsey-Henderson, A.E., Hawdon, A.A., Hairsine, P.B., Bartley, R., Baker, B., 2018. Grazing impacts on gully dynamics indicate approaches for gully erosion control in northeast Australia. Earth Surf. Process. Landf. 43 (8), 1711–1725. https://doi.org/10.1002/esp.4339.

Zebker, H.A., Villasenor, J., 1992. Decorrelation in interferometric radar echoes. IEEE Trans. Geosci. Remote Sens. 30, 950–959. https://doi.org/10.1109/36.175330.